Band gap analysis in MOF materials: Distinguishing direct and indirect transitions using UV–vis spectroscopy

Pedro Andrade, Christophe Volkringer, Thierry Loiseau, Antonio Tejeda, Matthieu Hureau, Alain Moissette

Applied Materials Today 37 (2024) 102094

Contents lists available at ScienceDirect

Applied Materials Today

journal homepage: www.elsevier.com/locate/apmt

Band gap analysis in MOF materials: Distinguishing direct and indirect transitions using UV–vis spectroscopy

Pedro H.M. Andrade [a,*], Christophe Volkringer [b], Thierry Loiseau [b], Antonio Tejeda [c], Matthieu Hureau [a], Alain Moissette [a]

[a] Laboratoire de Spectroscopie pour les Interactions, la Réactivité et l'Environnement (LASIRE), Université de Lille – Sciences et Technologies, Villeneuve d'Ascq 59655, France
[b] Unité de Catalyse et Chimie du Solide (UCCS), Univ. Lille, CNRS, Centrale Lille, Univ. Artois, UMR 8181, Villeneuve d'Ascq 59655, France
[c] Université Paris-Saclay, CNRS, Laboratoire de Physique des Solides, Orsay 91405, France

ARTICLE INFO

Keywords:
Band gap
MOF
Boltzmann regression
Kramers-Kronig
UV–vis

ABSTRACT

Metal-Organic Frameworks (MOFs) have gained considerable attention due to their potential applications in gas storage, separation, and catalysis. These porous materials exhibit properties of interest for semiconductor physics and homogeneous photocatalysis, in which concepts from coordination chemistry and semiconductor physics are often mixed. In the photocatalysis field, the optical band gap of the semiconductors is a crucial parameter that determine their functionality. Despite all the interest of MOFs, there is still a considerable lack of information about their band gap evaluation (especially if the gap is direct or indirect) using UV–Vis spectroscopy, and there is a considerable scattering in these values. The Tauc plot method is frequently used to access band gaps, even though it is not always accurate, especially for distinguishing direct and indirect band gaps. A more complete and precise analysis can be reached by using additional experimental techniques (XPS, UPS, and IPES spectroscopies), that are not always of easy access. This work examines several approaches for determining the band gap of MOF materials and proposes methodologies for a correct data interpretation, which leads to a better agreement between experimental and theoretical gaps. Several methods were analyzed to access the band gap of different MOF materials – UiO-66(Zr), UiO-66(Hf), UiO-66(Zr/Ti), UiO-66(Hf/Ti), UiO-67(Zr)_NH_2, UiO-67(Zr/Hf)_NH_2, UiO-67(Hf)_NH_2, MIL-125(Ti), and MIL-125(Ti)_NH_2 – purely from diffuse reflectance UV–vis (DR-UV–vis) data. The Kubelka-Munk and log(*1/R*) approaches were considered for transforming the DR-UV–vis spectra and the results demonstrate that the former method is more suitable, as it provides spectra with sharper absorption edges, which facilitates the interpretation and characterization of the optical band gaps. This study also highlights the importance of pre-data treatment and baseline correction in cases where a pre-absorption edge is present. Finally, by applying the Kramers-Kronig transformation to the reflectance spectra, and the Boltzmann regression to the Kubelka-Munk data, a solid base was created for determining if a material has a direct or an indirect gap. In addition, for some materials, the need for acquiring both the indirect and direct band gap values was discussed, as in some of these hybrid materials, both of these transitions can occur simultaneously. This paper guides the research community towards a most suitable methodology for assessing optical band gaps in hybrid materials, as it assists researchers in selecting the best methodology for their needs while avoiding typical mistakes in data interpretation.

1. Introduction

Heterogeneous photocatalysis has become a field of great interest since its early development back in the 70′s [1]. Since then, it has become a multidisciplinary area that incorporates semiconductor physics, surface sciences, physical chemistry, materials science, biology, and chemical engineering [2,3]. After the demonstration of the water photolysis in the presence of TiO_2 by Fujishima and Honda in 1972 [1], different types of semiconductors have been extensively evaluated according to their photocatalytic properties in liquid and gaseous mixtures, worth mentioning TiO_2, ZnO, Fe_2O_3, ZnS, and CdS [2,4]. Later on, many other materials and heterojunctions have been developed for

* Corresponding author.
E-mail address: pedro.moraisandrade@univ-lille.fr (P.H.M. Andrade).

https://doi.org/10.1016/j.apmt.2024.102094
Received 28 November 2023; Received in revised form 3 January 2024; Accepted 25 January 2024
Available online 10 February 2024

photocatalytic applications, such as polymers [5], Metal-Organic Frameworks (MOFs) [6], and MOFs-TiO_2 heterojunctions [7]. The properties of those materials – e.g., porosity, Specific Surface Area (SSA), particle size, and electronic structure – have been continuously improved over the years due to the extensive research in this field [8–10]. When considering the most common inorganic semiconductors, their main properties (such as electronic structure, band gap energies and types) are already thoroughly known, mainly due to the large number of experimental and theoretical data that have already been collected. On the other hand, due to the large number of MOFs that already exist and that are discovered daily (there are more than 90,000 MOF-structures documented in the Cambridge Structural Database and more than 500,000 have been predicted) [11,12], theoretical studies that normally take several months to be conducted cannot keep up with the speed in which new structures are discovered.

These hybrid, crystalline, porous materials have characteristics that are, in certain aspects, gathered between semiconductor physics and homogeneous photocatalysis. Consequently, they can be thought as solids with well-defined boundaries with the solution, but also as infinite quasi-molecules [13]. It is rather unusual how concepts of coordination chemistry are often mixed with those of semiconductor physics in MOFs literature [14]. This dual nature poses a challenge when addressing classical semiconductor characteristics, such as electrical conductivity – a crucial parameter for categorizing conductors, semiconductors, or insulator materials, which is not extensively explored in the context of MOF photocatalysis [14]. Classical inorganic semiconductors have conductivity in the range of 10^{-6} to 10^{4} $S.cm^{-1}$ [15–17]. In contrast, MOFs like UiO-66 (10^{-7} – 10^{-5} $S.cm^{-1}$) and MIL-100(Fe) (8.09×10^{-5} $S.cm^{-1}$) display significant lower values [18,19]. This discrepancy raises the question of whether some MOFs should be classified as insulators or semiconductors. It is crucial to recognize that, unlike classical semiconductors with densely packed crystal lattices and continuous pathways, MOFs electrical conductivity relies on charge transfer complexes between their organic and inorganic components [13]. Consequently, the charge carrier mobility is contingent upon the density and dynamics of these hopping states [14]. It should also be considered that the porous structure of MOFs establishes proximity between the photoactive sites and the target species, eliminating the need for charge carriers to migrate toward the material's external surface (as in most inorganic semiconductors). For this reason, MOF materials can often exhibit higher photoactivities than classical semiconductors even though their conductivity values are significantly smaller [20].

One of the most important characteristics of a semiconductor is whether its optical band gap exhibits a direct or an indirect transition, as this will have direct consequences over the electron-hole dynamics and reactivity upon photoexcitation [21]. Indeed, if a semiconductor has a direct band gap and the electric dipole transition from the valence band maximum (VBM) to the conduction band minimum (CBM) is allowed, the electron-hole pairs will recombine radiatively with a high probability [21]. On the other hand, the recombination is hampered in indirect band gap materials due to the momentum difference in the Brillouin zone between the VBM and the CBM [21]. Therefore, semiconductors with indirect band gap are expected to exhibit higher photoactivities when compared to those with direct gaps.

For inorganic semiconductors, this band gap is frequently obtained using the Tauc plot applied to the UV–vis data, and the nature of the transition greatly changes the obtained values [22]. However, approaches based purely on this method are not accurate in a general sense, especially for distinguishing direct and indirect band gaps. For dealing with this limitation, researchers often combine other experimental techniques to obtain this information, such as X-ray photoelectron spectroscopy (XPS), ultraviolet photoelectron spectroscopy (UPS), and inverse photoelectron spectroscopy (IPES) [23]. Nevertheless, these techniques are not always of easy access, which hinders a more complete and accurate analysis. For such reason, this paper draws attention to the several studies that have been conducted in the last few decades for assessing the electronic structure of Metal-Organic Frameworks. It also discusses the reliability of the obtained results and their respective methodologies, proposing a combination of methodologies for determining band gap energies and types purely from diffuse-reflectance UV–vis data, which should reduce the gap between experiment and theory in the MOF realm.

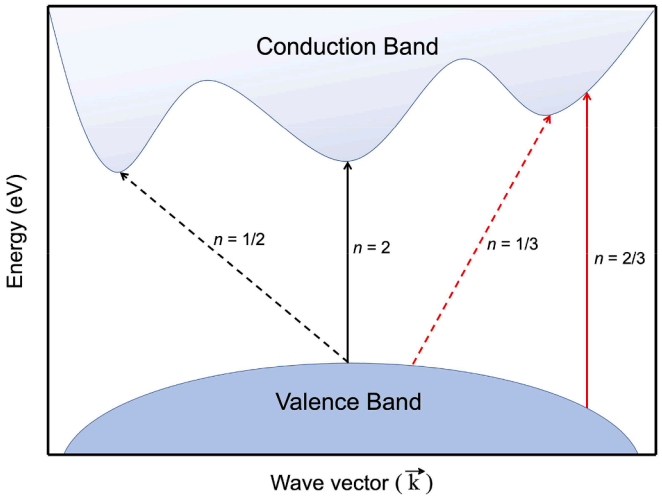

Fig. 1. Scheme showing the different types of optical transitions between the valence band and the conduction band in a semiconductor. In black: allowed transitions. In red: forbidden transitions. Solid arrows represent direct transitions and dotted arrows represent indirect ones. The coefficient n depends on the electron transition exhibited by the material – e.g., indirect allowed transition ($n = 1/2$), direct allowed transition ($n = 2$), indirect forbidden transition ($n = 1/3$), and direct forbidden transition ($n = 2/3$).

1.1. The band gap theory in UV–vis spectroscopy

Different classes of materials such as metals, semiconductors, and insulators can be distinguished by the energy distribution of their electronic states near the Fermi level E_F [24,25]. In metals and other conductive materials, the Fermi level lies inside at least one band; whereas in semiconductors and insulators it is situated in an energy range where no electronic state can exist [26]. This region, commonly known as band gap (E_g), refers to the energy difference (usually in eV) between the VBM and the CBM. In other words, it represents the minimum energy necessary ($E \geq E_g$) to promote an electron bounded to an atom to a conduction electron, which is free to move through the crystal lattice, serving as charge carrier.

For instance, semiconductors have the capacity to absorb photons with a certain amount of energy $h\nu \geq E_g$ and use it to excite electrons from the valence band (VB) to the conduction band (CB) [27]. Several studies were conducted aiming to obtain compounds with narrower band gaps, which allows the excitation of electrons within the visible light and near-IR region [28–31]. This feature is greatly desired for the environmental remediation of different pollutants since those materials can be photoactive under solar light, which guarantees a better reaction yield for compounds with reduced E_g [32]. However, wider band gaps are also envisaged in other applications, such as optoelectronic and energy harvesting [33]. For this reason, the assessment of the band gap energy of semiconductors is crucial to the study of such materials, especially in the photocatalysis field.

These optical transitions can present changes in the electron wavevector ($\vec{k}$) or not. Here, it is worth mentioning that direct and indirect transitions are characterized by the momentum difference in the Brillouin zone between the minimal-energy state in the CB and the maximal-energy state in the VB [34,35], as schematized in Fig. 1. If those states occur in different k-vectors, the material has an indirect

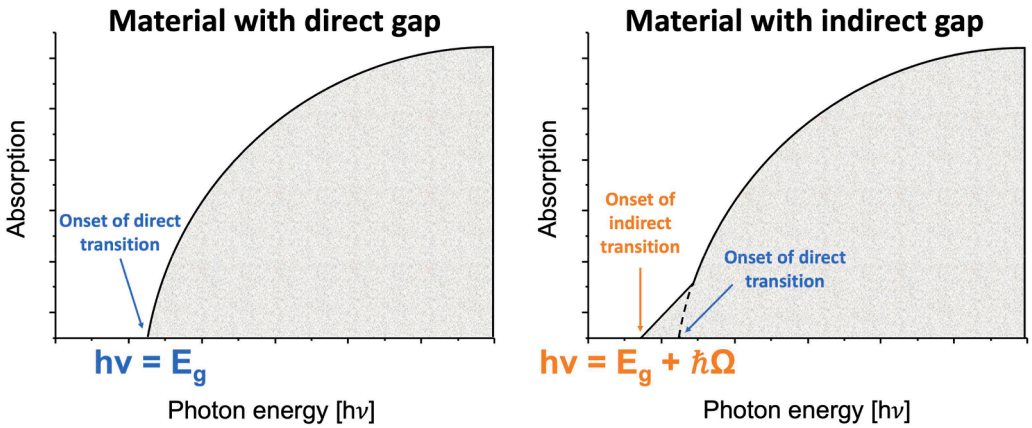

Fig. 2. Scheme representing the optical absorption spectra at 0 K for a crystalline material with direct (left) and indirect gaps (right). The energy for the onset of the direct transition is displayed in blue and for the indirect transition, in orange. Copyright © 2005 John Wiley & Sons, Inc. Used with permission from Ref. [38].

band gap and the transition is labeled as "phonon assisted", since almost all the change in the momentum of the system is transferred from a phonon [35]. On the other hand, if the momentum of the charge carriers is preserved, a direct band gap is ascribed to the compound and only photons are involved in the transition [35]. According to the selection rules for optical transitions [36,37], the transitions are allowed (higher probability) or forbidden (lower probability), which affects the measurements for quantifying E_g.

In an ideal scenario, at absolute zero temperature (with no phonons available), the optical absorption plotted versus the photon energy has a different behavior for crystals with direct and indirect gaps, as demonstrated in Fig. 2. At first, in materials with direct gaps, the band edge determines the gap energy as there is no significant change of $\vec{k}$ and therefore, $E_g = h\nu$ [38]. However, in indirect band gap materials, the band edges of the VB and CB are widely separated in the $\vec{k}$ space. For this reason, a phonon with energy $\hbar\Omega$ and wavevector $\vec{k}$ has to be emitted for the transition to take place. As a consequence, the optical absorption is weaker near the band edge [38]. In such systems, the energy necessary for the indirect process to occur is greater than the true band gap – as it needs to be partially used to emit a phonon – and the absorption threshold for the indirect transition between the VB and the CB is at $h\nu = E_g + \hbar\Omega$ (Fig. 2) [38]. Finally, at higher temperatures, if a phonon is absorbed along with a photon, the transition takes place at $h\nu = E_g - \hbar\Omega$ [38].

In both the direct and indirect band gaps, the absorption coefficient $\alpha(E)$ is expected to be zero for energy values smaller than the band gap of the material, as indicated in Eq. (1). For direct and indirect band gaps, there are significant differences in the relation between $\alpha(E)$ and E_g, as highlighted in Eqs. (2) and (3), respectively,

$$\alpha\left(E < E_g\right) = 0 \tag{1}$$

$$\alpha_{direct}\left(E \geq E_g\right) \propto \left(E - E_g\right)^{1/2} \tag{2}$$

$$\alpha_{indirect}\left(E \geq E_g\right) \propto \left(E + \hbar\Omega - E_g\right)^2 \tag{3}$$

where $\hbar\Omega$ represents the energy of a phonon. Due to these relationships, the band gaps can be determined by measuring the absorption coefficient. If the gap is direct, E_g can be assessed through the extrapolation of the linear least squares fit of α^2 in a "α^2 versus $h\nu$" plot that intercept the *x-axis* [34]. Similarly, if the band gap is indirect, E_g can be obtained by the extrapolation of the linear least squares fit of $\alpha^{1/2}$ to zero, in a "$\alpha^{1/2}$ versus $h\nu$" plot [34]. However, this semi-classical approach presents some failures at low temperatures (since no Coulomb attraction is taken into account), in materials presenting defects and impurities (due to extrinsic absorption), and for energies $E \gg E_g$ [34]. Also, some other effects such as local temperature [39], external strong electric or magnetic fields [40,41], and doping-alloying effects should be considered as they can influence the $\alpha(E)$ profiles [34].

When structural-electronic disorder is present (for amorphous semiconductors, for example), the determination of the band gap from optical absorption requires other methodology, especially due to the presence of tail states nearby the VB and the CB [34]. Such approach was first proposed by Tauc [42] by imposing some restrictions to the optical absorption processes, such as considering an absence of k-vector conservation, a constant momentum transition matrix element, and a density of electron states close to the VB and CB that is proportional to the square root of the photon energy. During the study, Tauc [42] evaluated the optical properties and the electronic structures of amorphous germanium, and showed that there are regions in which $\hbar\omega\sqrt{\varepsilon_2}$ is linearly dependent on the photon energy ($\hbar\omega$), where $\hbar$ is the reduced Plank constant (6.582×10^{-16} eV·s), ω is the photon angular frequency (rad.s^{-1}), and ε_2 is the imaginary part of the relative permittivity. ε_2 is defined according to the Eq. (4),

$$\varepsilon_2 = 2n\kappa \tag{4}$$

in which n is the refractive index and κ is the extinction coefficient. In this context, Tauc et al. [42] verified an absorption band represented by a straight line where $\omega^2\varepsilon_2 \approx (\hbar\omega - E_g)^2$. They demonstrated that the band gap of the material can be obtained through the intercept between the extrapolation of this line and the photon-energy axis. The authors also verified that in this case only the energy is conserved (electron and photon) but not the momentum (k-vector), which is indicative of an indirect transition [42].

The optical and electronic properties of amorphous semiconductors were further investigated by Davis and Mott in more general systems [43]. They proposed a relationship that offered the best fit to the optical absorption edge by considering the conductivity σ at a certain angular frequency ω, according to the Eq. (5). Then, from the plot of $(\alpha\hbar\omega)^2$ against the photon energy $\hbar\omega$, where α is the absorption coefficient (cm^{-1}), a linear region was obtained and extrapolated to the abscissa axis to assess the E_g value.

$$\sigma(\omega) = \frac{\sigma_0\left(\hbar\omega - E_g\right)^2}{\hbar\omega} \tag{5}$$

A relation was further stablished between the measured absorbance and the energy, showing that the optical absorption strength depends on the difference between the photon and the band gap energy as represented in Eq. (6) [44]. In this case, h is the Plank constant (4.1357×10^{-15} eV.s), ν is the photon frequency (Hz), A is the slope of the Tauc plot in the linear region, and n depends on the electron transition exhibited by the material (Fig. 1) – e.g., indirect allowed transition ($n =$

Table 1
Available methods for obtaining the absorption coefficient (α) using UV–vis data. d is the thickness of the sample, T is the transmittance, R is the reflectance, R_∞ is the diffuse reflectivity of a non-absorbing material, K and S are the Kubelka-Munk absorption and scattering coefficients, respectively.

Method	Formula	Considerations
Bouger-Lambert-Beer [52–54]	$\alpha_{BLB}(E) = \frac{1}{d}\ln\left(\frac{1}{T}\right)$	Does not consider the reflectance
Pankove [55]	$\alpha_P(E) = \frac{1}{d}\ln\left[\frac{(1-R)^2}{T}\right]$	Considers that the product αd is large
Pankove-Vahalová [55, 56]	$\alpha_{PV}(E) = \frac{1}{d}\ln\left[\frac{(1-R)^2}{T} + \sqrt{\frac{(1-R)^4}{4T^2} + R^2}\right]$	Includes internal reflections for small values of αd
Kubelka-Munk [57]	$\alpha_{KM}(E) \cong F(R) = \frac{(1-R_\infty)^2}{2R_\infty} = \frac{K}{S}$	Considers a two-flux radiation model

1/2), direct allowed transition ($n = 2$), indirect forbidden transition (1/3), and direct forbidden transition (2/3).

$$(\alpha h\nu)^n = A\left(h\nu - E_g\right) \tag{6}$$

Although the Tauc method was originally developed for the evaluation of absorption in amorphous semiconductors, it is extensively applied for assessing the band gap of crystalline thin films [44] and nowadays, it is commonly used for other types of crystalline materials as well – such as powdered TiO_2 and ZnO [45–47]. Dolgonos, Mason, and Poeppelmeier [48] emphasized that the Tauc plot is only applicable to materials in which a localization of energy states can be assumed (which is the case of amorphous materials and nanoparticles), indicating that the method is inappropriate to deal with crystalline and/or highly-doped semiconductors. However, a recent study demonstrated that the linearity of the Tauc plot obtained for nanocrystals is not as significant when compared to that of bulk materials [45]. This last feature was ascribed to the discretization and blueshift of the energy spectrum from the electronic states, but also to the relaxation of the momentum selection rule which cannot be considered for crystals with considerably small size [45].

The usual procedure for a Tauc analysis consists in acquiring optical absorbance data and plotting $(\alpha h\nu)^n$ versus $h\nu$, while testing the n-values ($n = 2$ or ½) until the best fit is obtained for the absorption edge, allowing to assign the correct type of the optical transition to the material [44]. This analysis is not always obvious. The assignment is often difficult for materials with flat bands and, even sometimes for materials with dispersing bands [49]. In addition, some compounds present a pre-edge absorption in their UV–vis spectra, which can influence the interpretation and the accuracy of the band gap estimation [50]. Also, Coulter and Birnie [44] highlighted that materials that exhibit indirect band gaps may also present direct transitions at higher energies, which would justify the acquisition of both E_g values (for $n = 2$ and ½). This means that both direct and indirect transitions can happen in all semiconductor materials if the energetic conditions are favorable [47].

In view of all the previously mentioned situation that led to deviations from the Tauc theory, other methodologies have been proposed for assessing the band gap energies from UV–vis data. For instance, Cody et al. [51] adopted a methodology that assumes a constant dipole transition matrix element, where E_g is obtained from the extrapolation of the linear least squares fit of $(\alpha/h\nu)^{1/2}$ to zero in a "$(\alpha/h\nu)^{1/2}$ versus $h\nu$" plot (normally, $E_{Tauc} > E_{Cody}$). Another approach was proposed by Zanatta [34], which reported a method to obtain E_g by fitting a sigmoid (Boltzmann) function to the optical absorption spectra of crystalline (plate-like and powdered samples) and amorphous Ge, Si, and GaAs compounds. In that study it was concluded that, regardless of the method, the absorption coefficient (α) or absorbance is one of the most important physical parameters for evaluating the band gap. Table 1 shows precisely that the band gap values are independent of the model.

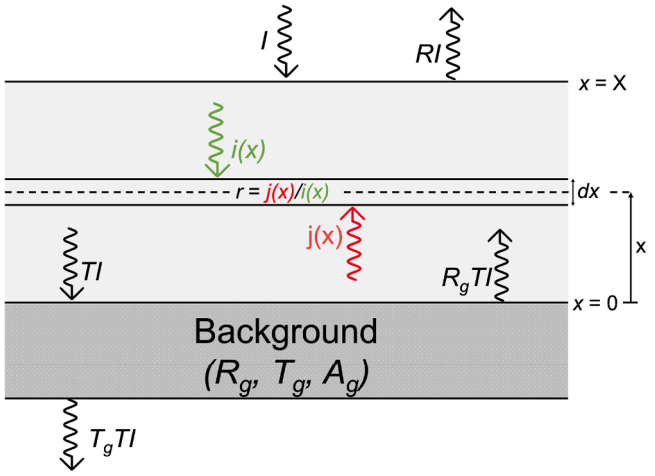

Fig. 3. Scheme of the Kubelka-Munk model for the reflectance and transmittance of a finite thick plane-parallel light-scattering specimen (thickness ≡ X) placed in contact with a background substrate with known reflectance (R_g), transmittance (T_g) and absorbance ($A_g = 1 - T_g - R_g$). I is the intensity of the incident radiation, $i(x)$ is the light flux that flows through the illuminated surface, $j(x)$ is the light flux flowing back to the illuminated surface, T is the fraction of the incident light transmitted by the substrate, and R is the total reflectance of the system.

Other techniques can be also combined for evaluating the band gap of semiconductors [14]. For instance, the VBM can be obtained by combining X-ray photoelectron spectroscopy (XPS), ultraviolet photoelectron spectroscopy (UPS), and photoelectron spectroscopy in air (PESA); while the CBM can be assessed through inverse photoelectron spectroscopy (IPES) [23,58–61].

1.2. The link between absorption and diffuse reflectance

The Kubelka-Munk theory is the most applied method for obtaining "absorbance" spectra from diffuse reflectance data [57]. The model is based on a radiation field inside a light-scattering sample, where two fluxes cross an arbitrary section (dx) in opposite directions (Fig. 3) [62]. In fact, the well-known K-M function – $F(R_\infty)$ – was obtained by applying some boundary conditions to this system (such as considering samples as infinity thick), resulting in Eq. (7) [63].

$$F(R_\infty) = \frac{(1-R_\infty)^2}{2R_\infty} = \frac{K}{S} \tag{7}$$

The Kubelka-Munk transform is regularly used in solid-state spectroscopy measurements as, in this case, the samples are often opaque and can be considered as an infinitely thick coating [47,64]. However, for diffuse reflectance UV–vis spectroscopy the samples are regularly measured in their natural particulate state. Thus, this previous assumption becomes incorrect and higher deviations from linearity are observed [65]. In fact, the K-M theory exhibits high deviations from experimental data when the reflectance values are below 60 % ($K/S >$ 0.13) [66]. For instance, Landi et al. [67] demonstrated that a thickness of about 0.5 mm is not sufficient for applying the K-M function in diffuse reflectance UV–vis data acquired for TiO_2 nanoparticles. However, even though the Kubelka-Munk theory is considered as a pseudo-absorption function [34], it is widely accepted nowadays for evaluating the band gap energies of most semiconductor materials through diffuse reflectance UV–vis measurements [47]. On the other hand, in several cases, researchers use the $\log(1/R)$ function as an empirical pretreatment to the data in order to normalize it [65].

1.3. Assessment of the band gap energy in MOF materials

MOFs are a relatively new class of materials, composed by inorganic clusters connected to each other by organic linkers thus, forming a hybrid crystalline structure with high porosity and high Specific Surface Areas (SSAs) [68]. One of the most interesting features of MOFs is the possibility of chemically modifying them, either by decorating their pores with nanoparticles, by functionalizing their linkers with different organic groups, by replacing their metal sites, or even by creating defects on their structures [68]. These characteristics, coupled with the enormous possibilities of combining different organic linkers and metal sites, allow the formation of several structures with distinct charge transfer complexes (CTC) upon UV–vis excitation – considering the inorganic cluster, the organic linker, and other guest species. For instance, Linker-Based Transition (LBT) [69,70], Metal-Based Transition (MBT) [71], Linker-to-Linker Charge Transfer (LLCT) [72], Metal-to-Metal Charge Transfer (MMCT) [73], Metal-to-Linker Charge Transfer (MLCT) [74], and Linker-to-Metal Charge Transfer (LMCT) [69] are some of these CTC that were already observed in different MOF systems.

When dealing with these hybrid materials in photocatalysis, the concepts between semiconductor physics and homogeneous photocatalysis are often mixed [14]. Kolobov, Goesten, and Gascon [14] highlighted how unusual it is to mix coordination chemistry notions (such as LMCT) to others from semiconductors physics (such as conduction band) as it happens in MOFs literature. However, this happens because of the dual character of these hybrid materials. For instance, the alignment of the electronic bands in MOFs (semiconductor physics) can be manipulated by functionalizing their linkers (coordination chemistry), similarly to what occurs in solution [75]. The proximity of the MOFs from the solution state lies specially on the fact that these materials have a great volume of pores which are, routinely, filled with solvent molecules [14]. However, in some cases, they can also behave like nonmolecular semiconductors in photovoltaics, especially when considering their curvature maxima (VBM and CBM) and also their conductivity, even though this last feature is not much explored in the field of MOFs photocatalysis [14]. For these reasons, some concepts were adapted for dealing with such systems, worth mentioning the use of HOCO (Highest Occupied Crystalline Orbital) and LUCO (Lowest Unoccupied Crystalline Orbital) instead of the well-known nomenclatures used for molecules (HOMO – Highest Occupied Molecular Orbital – and LUMO – Lowest Unoccupied Molecular Orbital) [69].

Due to the wealth of topologies and electronic structures in MOFs, they are particularly well-adapted compounds to study the procedures for determining band gaps. Several MOFs were synthesized during this work – UiO-66(Zr), UiO-66(Hf), UiO-66(Zr/Ti), UiO-66(Hf/Ti), UiO-67(Zr)_NH_2, UiO-67(Hf)_NH_2, UiO-67(Zr/Hf)_NH_2, MIL-125(Ti), and MIL-125(Ti)_NH_2 – and characterized by XRD and diffuse reflectance UV–vis spectroscopy. Other structural characterizations were conducted in previous works, worth mentioning N_2 sorption isotherms, Raman, FTIR, and EPR spectroscopies [70,76,77]. The band gap energies were assessed by different methods and the obtained results were further compared with other reports found in the literature.

2. Materials and methods

Syntheses: The synthesis procedures for all the MOFs presented here are described in the Supporting Information file.

X-ray diffraction: Powder X-ray Diffraction (PXRD) experiments were done using a SmartLab Rigaku diffractometer equipped with a 9 kW rotating anode X-ray generator (Cu $K\alpha_1 = 1.5418$ Å), endowed with a HyPix-3000 hybrid multi-dimensional pixel detector, using capillaries in parallel transmission geometry. The 2θ scans were performed in the range 5°−50°, with a step size of 0.01°, and a speed of 3°/min. Single crystal X-Ray Diffraction experiments were done using a Bruker Kappa Apex Duo diffractometer equipped with a two-dimensional CCD 4 K detector and 2 m-sources (Mo and Cu).

Table 2
Textural and physical chemical properties of the compounds synthesized in this work displaying the atomic ratio, the crystallite size, the $SSA_{(BET)}$, and the microporous volume.

MOF	Metal content ICP-OES	Crystal size μm	$SSA_{(BET)}$ ($m^2.g^{-1}$)	Microporous volume ($cm^3.g^{-1}$)
UiO-66(Zr)	100 $\%_{at}$ Zr	0.10 – 0.25	1262 ± 33	0.60(3)
UiO-66(Hf)	100 $\%_{at}$ Hf	0.18 – 3.33	828 ± 24	0.41(3)
UiO-66(Zr/Ti)	95.0 $\%_{at}$ Zr 5.0 $\%_{at}$ Ti	0.10 – 0.25	1342 ± 28	0.47(5)
UiO-66(Hf/Ti)	91.0 $\%_{at}$ Hf 9.0 $\%_{at}$ Ti	0.20 – 0.34	818 ± 20	0.30(9)
UiO-67(Zr)_NH_2	100 $\%_{at}$ Zr	32 – 51	1329 ± 36	0.68(4)
UiO-67(Zr/Hf)_NH_2	40.0 $\%_{at}$ Zr 60.0 $\%_{at}$ Hf	105 – 140	1234 ± 34	0.65(7)
UiO-67(Hf)_NH_2	100 $\%_{at}$ Hf	24 – 44	914 ± 25	0.48(4)
MIL-125(Ti)	100 $\%_{at}$ Ti	0.76 – 1.32	1207 ± 34	0.60(4)
MIL-125(Ti)_NH_2	100 $\%_{at}$ Ti	3.2 – 5.3	1099 ± 26	0.51(4)

Inductively coupled plasma - optical emission spectrometry: Inductively coupled plasma - optical emission spectrometry (ICP-OES) experiments were conducted using an Agilent 5110 ICP-OES spectrometer in radial sighting mode. The mineralization of the samples was performed using 100 mg of the activated UiO-66 compounds. First, the powdered samples were digested using a solution containing 10 mL of HF and 5 mL of HNO_3 and then they were heated to 140 °C for 48 h, followed by a dry evaporation step. Next, they were etched with aqua regia (HNO_3:HCl 3:6 mL), heated to 120 °C for 24 h and dried to a residue of 0.5 mL Finally, 9.5 mL of water was added and, after filtration, the solution was diluted at 1/100 before being analyzed.

Surface area measurement: N_2 sorption was performed at liquid nitrogen temperature (77 K) using a Micromeritics ASAP2020 apparatus. UiO-66, UiO-67_NH_2, MIL-125, and MIL-125_NH_2 samples were previously degassed under vacuum at 150, 60, 200, and 100 °C, respectively. The specific surface area and pore size distribution of the examined samples were evaluated by the multipoint BET (Brunauer–Emmett–Teller) model in the 0.02–0.3 p/p_0 range.

Scanning Electron Microscopy: SEM was conducted on a FEG microscope (Hitachi SU 5000) at an accelerating voltage of 5 kV, using samples previously sputter-coated with carbon.

Infrared spectroscopy: FTIR was performed on a Perkin Elmer Spectrum 2 spectrometer using an attenuated total reflectance (ATR) accessory and a diamond crystal as the reflective element. The spectra were taken at a resolution of 4 cm^{-1} and 128 scans.

Nuclear magnetic resonance spectroscopy: Liquid ^1H NMR spectroscopy was performed in a Bruker AVANCE III HD 300 MHz spectrometer via a 60-position Sample Xpress autosampler. The chemical shifts were referenced by the external resonance of the tetramethylsilane. The sample digestion was performed using 10 mg of the UiO-66 compounds. The material was soaked into 1 mL of a 4 M NaOD/D_2O solution and sonicated for 15 min. Then, 0.6 mL of the liquid was recovered by filtration and placed into a 5 mm NMR tube before being analysed at 8 scans.

Diffuse reflectance UV–vis spectroscopy: The UV–vis experiments were carried out on a Varian Cary 5000 spectrometer using Praying Mantis™ Diffuse Reflection Accessory adapted for the characterization of powder samples. The spectra were recorded in the 200–800 nm spectral range with a resolution of 1 nm. The diffuse reflectance spectra were plotted as well as the $\log(1/R)$ and the Kubelka-Munk function.

Band gap evaluation: The band gap energies were first evaluated by diffuse reflectance UV–vis spectroscopy. E_g was estimated by different

methods, worth mentioning the extrapolation of the diffuse reflectance curve R [34], the extrapolation of the K-M curve F(R), the extrapolation of the log*(1/R)* curve, the Cody's band gap [51] [$(\alpha/h\nu)^{1/2}$ versus $h\nu$], the indirect band gap [$\alpha^{1/2}$ versus $h\nu$] [34], the direct band gap [α^2 versus $h\nu$] [34], the Tauc's indirect band gap [$(\alpha h\nu)^{1/2}$ versus $h\nu$] [42], the direct version of Tauc's band gap [$(\alpha h\nu)^2$ versus $h\nu$] [35], and the sigmoid-Boltzmann function [34]. The E_g values were also determined using the Kramers–Kronig transformation from the UV–vis raw data.

3. Results and discussion

3.1. Characterization of the pristine materials

For facilitating the discussion of this paper, the main properties of the materials obtained here are displayed in Table 2. The quality of the synthesized MOFs was characterized by their PXRD patterns (Fig. S2), crystallographic parameters (Tables S2–S4), ICP-OES (Table 2), N_2 sorption (Fig. S3), SEM images (Fig. S4), FTIR spectroscopy (Fig. S5), and liquid ^{1}H NMR (Fig. S6). These characterizations were all in accord with other works from the literature, showing that the compounds were successfully synthesized. Most compounds exhibited type-I isotherms according to IUPAC classification, which is characteristic of microporous materials. UiO-66(Hf/Ti) exhibited a mixture of type-I and type-IV isotherms, indicating the presence of mesoporosity within the compound. This effect can be related to the agglomeration of the nanoparticles and to defect formation. The SSA values are all in accord with previous reports from literature [78–82]: UiO-66(Zr) = 1262 $m^2.g^{-1}$, UiO-66(Hf) = 828 $m^2.g^{-1}$, UiO-66(Zr/Ti) = 1342 $m^2.g^{-1}$, UiO-66 (Hf/Ti) = 818 $m^2.g^{-1}$, UiO-67(Zr)_NH_2 = 1329 $m^2.g^{-1}$, UiO-67(Zr/Hf) _NH_2 = 1234 $m^2.g^{-1}$, UiO-67(Hf)_NH_2 = 914 $m^2.g^{-1}$, MIL-125(Ti) = 1207 $m^2.g^{-1}$, and MIL-125(Ti)_NH_2 = 1099 $m^2.g^{-1}$. SEM images of UiO-66 and UiO-67 materials show crystal morphology of typical aggregates with octahedral shapes that are characteristic of these compounds [79,83]. MIL-125(Ti) exhibited crystallites that are analogous to truncated square pyramidal morphology and MIL-125(Ti)_NH_2 formed tetragonal plate shapes, which are also characteristic of these materials [80,84]. FTIR spectroscopy was able to identify different vibrational modes for the nine compounds. Their spectra can be divided into three regions: from 400 to 700 cm^{-1}, where the absorption bands are mostly related to inorganic cluster vibrations; from 700 to 900 cm^{-1}, where the interaction between the organic linker and inorganic node is observed; and from 900 to 1800 cm^{-1}, where only organic linker vibrations are active. Because UiO-66 solids are characterized by the presence of structural defects that may affect the UV–vis absorption features, the missing BDC linker content was evaluated using liquid ^{1}H NMR spectroscopy (Fig. S6). Actually, the formate (coming from the deprotonation of formic acid used as modulator in the syntheses process and also from the degradation of DMF) is able to partially substitute the BDC linker by generating defects of organic ditopic linkers. When a dicarboxylate linker is removed from the UiO-66 structure, it leaves the coordinating site with metallic centers available for two monotopic formate molecules instead. Considering these two types of coordination modes (monotopic versus ditopic), if the molecular formula for the pristine UiO-66 compound is represented by [$M_6O_4(OH)_4L_6$] (L = BDC), the absence of x ditopic linkers creates $2x$ carboxylate defects. Therefore, considering the presence of formate (F), the experimental molecular formula must be written as [$M_6O_4(OH)_4(L)_{6-x}(F)_{2x}$]. With that in mind, the integration of the NMR signal related to the formic acid was compared to that of the BDC linker for the four UiO-66 compounds. The UiO-66(Zr), UiO-66(Hf), UiO-66(Zr/Ti), and UiO-66(Hf/Ti) samples were found to exhibit 9.5, 7.0, 11.2, and 11.2 % of missing BDC linkers, respectively (Fig. S6). These results show that the number of defects in the samples increase in the presence of titanium. Similar characterizations were performed in a previous work using the UiO-67_NH_2 samples, for which no correlation between the structural defects and the metal content was observed [76].

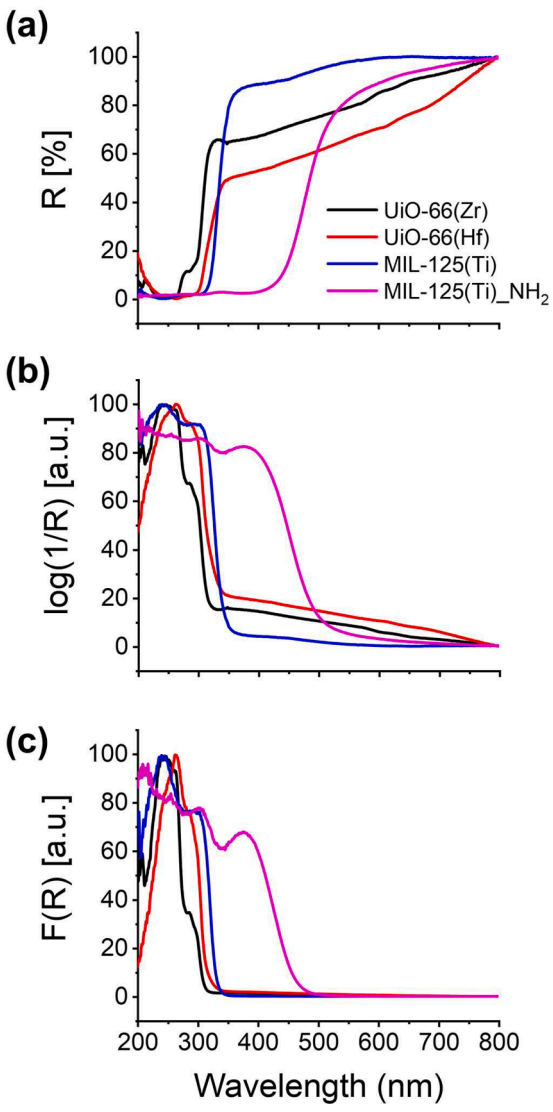

Fig. 4. (a) diffuse reflectance UV–vis, (b) log(1/R), and (c) Kubelka-Munk data obtained for UiO-66(Zr), UiO-66(Hf), MIL-125(Ti), and MIL-125(Ti)_NH_2. The log(1/R) and the F(R) spectra were normalized between 0 and 100 for comparative purposes.

3.2. Diffuse reflectance UV–vis spectroscopy

The diffuse reflectance UV–vis spectra obtained for the pristine MOFs synthesized in this work are displayed in Figs. 4 and S7, alongside the log*(1/R)* and the Kubelka-Munk representation. All the spectra were normalized from 0 to 100 for comparative purposes. The differences when evaluating the diffuse reflectance spectra using the K-M approach and the log*(1/R)* are clearly visible (Figs. 4, and S7). For instance, regarding the UiO-66 family, the K-M values present a thinner absorption band (between 200 and 320 nm) and a greater slope near its absorption tail when compared to the log*(1/R)* data. A similar feature is also present in the spectra of the UiO-67_NH_2, and MIL-125 compounds. This simple difference can, by itself, be a source of misevaluation of the materials' band gaps, as the extrapolation of these curves to zero (R, F (R), and log*(1/R)* versus $h\nu$) intercepts the abscissa axis in different $h\nu$ values. Moreover, it seems that the K-M method led to spectra that are more consistent when considering their absorption band edges, which are better delimited than those obtained by using the log*(1/R)* data. Nevertheless, because it is not possible to acquire absorption and transmission UV–vis data for powdered samples without pre-treatment,

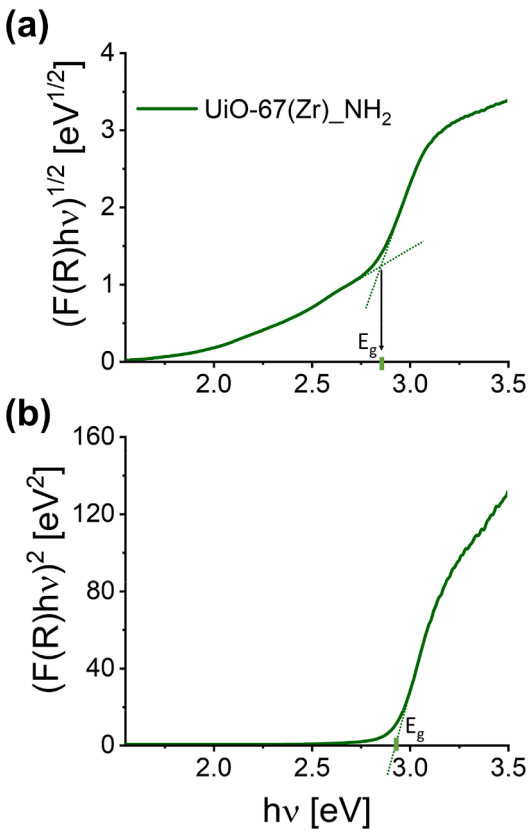

Fig. 5. Demonstration of how to assess the band gap value using the extrapolation of the curve obtained from the absorption band recorded for UiO-67(Zr)_NH_2. (a) indirect band gap with baseline correction; (b) direct band gap without baseline correction.

the K-M and the log*(1/R)* approaches are the best possible approximations for the *α(E)* in this work.

3.3. Band gap evaluation: Cody, Tauc, and direct/indirect methods

When evaluating the UV–vis spectra of different semiconductors, it is common to come across materials that exhibit a sub-band gap energy – especially in the case of defected, doped, bulk or surface modified materials. These modifications create intra-band gap states that reflect in their absorption spectra by forming an Urbach-like tail, which influences the band gap assessment by different methods [50]. In these cases, the curves need a baseline correction before being evaluated at the *x*-axis intercept point, as discussed by Makuła, Pacia, and Macyk [50]. This conclusion was reached by studying a dye modified TiO_2 semiconductor, where the system was measured by placing barium sulfate mixtures grounded separately with titania and methyl orange [50]. In a first step, these mixtures were placed side by side in the holder and then, in a second step, they were mixed and evaluated in a system where both components can interact [50]. In this last case, the authors verified that the resulting spectrum is not a simple sum of the individual spectra, but a linear combination of both [50]. This result can be extrapolated to hybrid materials as their different components (in this case the inorganic clusters and organic linkers) can lead to a spectrum whose contributions cannot be fully resolved. This feature can be easily identified in the spectra as, in these cases, the curves exhibit a smooth rise from the *x*-axis before reaching the linear region. On the other hand, the baseline correction is not necessary if the linear region appears right after a sudden rise of the curve from the abscises axis. Hence, a pre-treatment must be conducted in the cases where the compound presents a pre-absorption edge, as represented in Fig. 5. The Tauc plots obtained

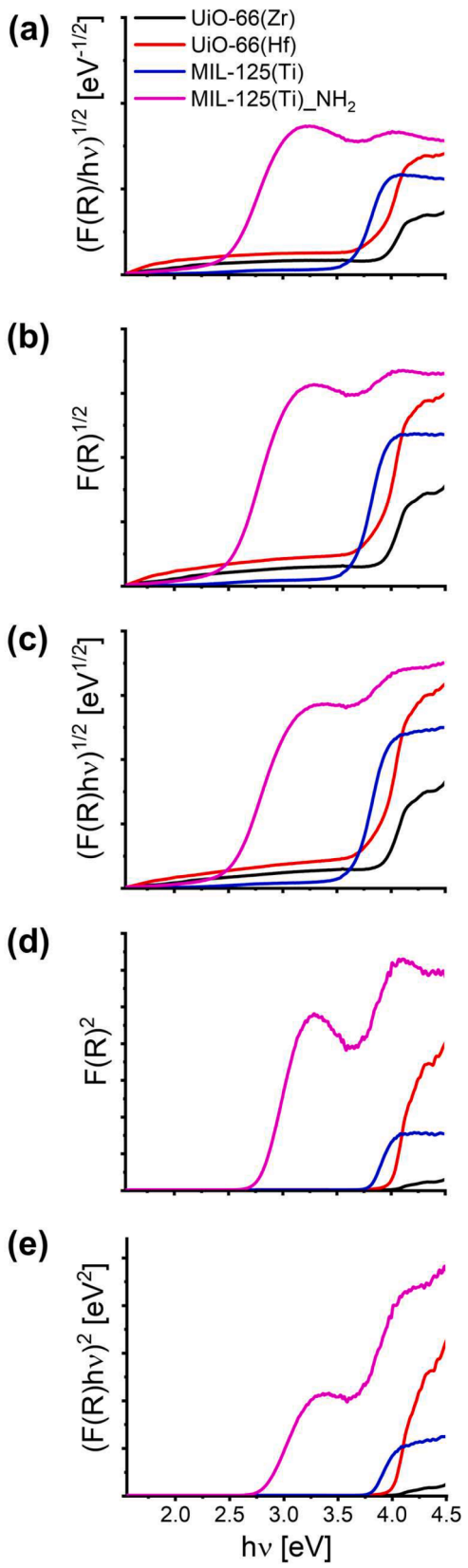

Fig. 6. Band gap energies assessment using the Kubelka-Munk function for UiO-66(Zr), UiO-66(Hf), MIL-125(Ti), and MIL-125(Ti)_NH_2 materials. (a) Cody band gap; (b) indirect band gap; (c) Tauc indirect band gap; (d) direct band gap; (e) Tauc direct band gap.

Table 3
Band gap values (eV) assessed through the plot of R, F(R), $(F(R)/h\nu)^{1/2}$, $F(R)^{1/2}$, $(F(R)h\nu)^{1/2}$, $F(R)^2$, and $(F(R)h\nu)^2$ versus the photon energy hν.

Method	UiO-66				UiO-67_NH_2			MIL-125	
	Zr	Hf	Zr/Ti	Hf/Ti	Zr	Zr/Hf	Hf	H	NH_2
R	4.20	4.14	4.09	3.97	3.08	3.04	3.08	3.88	3.00
F(R)	3.98	3.93	3.89	3.94	2.83	2.88	2.90	3.75	2.69
$(F(R)/h\nu)^{1/2}$	3.95	3.88	3.74	3.74	2.84	2.89	2.92	3.67	2.54
$F(R)^{1/2}$	3.96	3.89	3.78	3.79	2.85	2.92	2.90	3.67	2.52
$(F(R)h\nu)^{1/2}$	3.96	3.90	3.79	3.82	2.85	2.91	2.92	3.67	2.53
$F(R)^2$	4.05	4.04	4.00	4.04	2.92	2.95	2.98	3.82	2.80
$(F(R)h\nu)^2$	4.06	4.03	4.02	4.05	2.93	2.96	2.98	3.81	2.80

from UiO-67(Zr)_NH_2 absorption band exhibit a linear region when considering both indirect (Fig. 5a) and direct (Fig. 5b) band gaps. However, to guarantee a better fitting of the Tauc function, it should be noted that a baseline correction is required before the extrapolation of the curve in the case of indirect band gap. In order to do this, a tangent line is traced to the curve in the region just before the linear region of the indirect plot. The band gap value is then assessed using the *x* position of the intercept between this tangent line and the one coming from the linear region (Fig. 5a). This correction is also needed for the Cody band gap and for the direct $[F(R)^2]$ and indirect $[F(R)^{1/2}]$ methods.

To determine if a compound has a direct or an indirect band gap in the absence of calculations, it is recommended to plot both the direct and indirect band gaps as a function of the photon energy [34]. The plot exhibiting a clear linear region should be considered as the best fitting and therefore, is presumed to be the correct band gap type [34]. A difference on the optical absorption spectra may also report if a material displays a direct or an indirect gap. In fact, for direct gaps, there is a sudden step rise in absorption (see spectra of UiO-66 compounds in Figs. 4 and S7), whereas for indirect gaps there is first a small gradual rise in a frequency range, followed by a sudden rise in absorption (see spectra of MIL-125(Ti)_NH_2 in Fig. 4) [85]. In this last case, the frequency at which the absorption coefficient starts rising gradually is the measure of the indirect gap [85]. However, this determination is not as simple as it seems. For instance, the electronic structure of the UiO-66 compound has been deeply evaluated in different works and it was concluded that UiO-66(Zr) exhibits a direct band gap [86,87]. This observation was further confirmed by Yasin et al. [88], who found by DFT calculations and experiments that substituting zirconium by hafnium in UiO-66 does not change the band gap type, which is direct regardless the metal. Still, it is possible to find several studies that consider the UiO-66 materials as presenting an indirect band gap [89, 90]. These controversies are especially common in the realm of MOFs, since most of these compounds exhibit linear regions regardless the type of plot (direct or indirect) that is considered (Figs. 6, S8, and S9). This feature demonstrates the necessity to consolidate a method to determine if a material has a direct or an indirect band gap only by means of experimental data. Aiming to address this issue, the band gap energies of the MOFs synthesized here were assessed using different approaches by means of the Kubelka-Munk function, as represented in Table 3 and in Figs. 6 and S8. In this case, the band gap was accessed from the tangent line to the absorption band edge until it intercepts the abscissa axis at the E_g value. In the case of Tauc indirect band gap, Cody band gap, and indirect band gap, a baseline was first considered as discussed before (Fig. 5a). Note that it is mandatory that the *y*-axis starts at zero.

It is reasonable to assume that the first electronic transition observed in a UV–vis spectrum starting from lower to higher energies (in other words, from higher to lower wavelengths) corresponds to the HOCO – LUCO transition in crystalline materials [69]. For this reason, it is possible to extrapolate the tangent line to the absorption band edge until it intercepts the abscissa axis and then, transform the wavelength value to electron-volts to find the E_g value for the material. This result is highlighted in Table 3 as F(R) method ($E_{g[F(R)]}$). This approach was conducted elsewhere for MIL-100(Al), and the band gap type was found to be indirect due to the proximity between the $E_{g[F(R)]}$ and the $E_{g(ind)}$ values [7]. In MOF systems, this is a more accurate approach than the others presented before, as it relies only on the experimental data and not on partial assumptions (i.e., the best linearity or different step rise in absorption UV–vis data). Interestingly, these $E_{g[F(R)]}$ values are in between the indirect and the direct band gaps for all the compounds studied here (i.e., $E_{g[F(R)]\_MIL\text{-}125(Ti)} = 3.75$ eV, $E_{g(dir)\_MIL\text{-}125(Ti)} = 3.67$ eV and $E_{g(ind)\_MIL\text{-}125(Ti)} = 3.82$ eV) [87].

When considering the band gap for UiO-66 samples, all methods end up generating plots with linear regions between 3.5 and 4.5 eV. The values obtained using the Cody, the indirect, and the Tauc indirect methods exhibit a pre-absorption edge and therefore, must be corrected by a baseline – which is also the case for UiO-67_NH_2 and MIL-125 compounds (Figs. 6, S8, and S9). As mentioned before, some works in the literature consider that UiO-66 exhibits a direct band gap, while others assume that it behaves as an indirect semiconductor. In fact, the Tauc direct band gap value for UiO-66(Zr) matches to that obtained from DFT simulations (4.07 eV) [87] and also from experimental data (4.07 eV) [79]. On the other hand, the UiO-66(Zr) Tauc indirect band gap is also similar to that found through experimental UV–vis data elsewhere [90]. Therefore, the acquisition of both direct and indirect values is justified in this case [86,87,89,90].

Other works demonstrate that the presence of hafnium and/or titanium reduces the band gap of the UiO-66 materials [70,89]. However, in the presence of hafnium or titanium, DFT simulations are not as accurate as for the zirconium-based material. In fact, the Tauc direct E_g found for the hafnium-based UiO-66(Hf) using computational data (3.74 eV) [87] is smaller than that obtained from diffuse reflectance UV–vis spectroscopy in this work (4.03 eV) and in previous studies [70]. This feature demonstrates how theoretical band gap calculation can considerably differ from experimental data in many compounds. For instance, the predicted band gap value for a 100 at.% titanium-based UiO-66(Ti) was found to be 3.64 eV [87], which is smaller than the energies obtained in this study using the Tauc method: UiO-66(Zr/Ti) = 3.79 eV and UiO-66 (Hf/Ti) = 3.82 eV. Other works also reported similar experimental values for the band gap of UiO-66(Zr/Ti) material [90].

UiO-67 is another compound that has been found both as direct or indirect semiconductor in different studies [91,92]. It is also a good example of how the Tauc plot can provide a different evaluation of the band gap than other methods. For example, if the baseline correction is not applied to the indirect Tauc plot data, the band gap is found to be around 2.0 eV for UiO-67 [91], which is very different from the predicted value using computational simulation (~ 3.7 eV) [87,93] and also from the experimental one (3.68 eV) [94]. Wang et al. [95] accessed the experimental band gaps for a series of zirconium-based UiO-6*x*_NH_2 (*x* = 6, 7, or 8) and using the Tauc plot found a direct band gap of 2.76 eV for UiO-67(Zr)_NH_2, which is close to the value obtained here (Table 3). Contrary to what was observed for UiO-66 [70], the presence of hafnium does not have a great influence on the calculated band gap values for the UiO-67_NH_2 samples [76], which can even increase from 2.93 to 2.98 eV when replacing zirconium by hafnium (Table 3). This different behavior is ascribed to a change on the valence band electronic states caused by the presence of the amino group [88]. In fact, replacing Zr by Hf cations

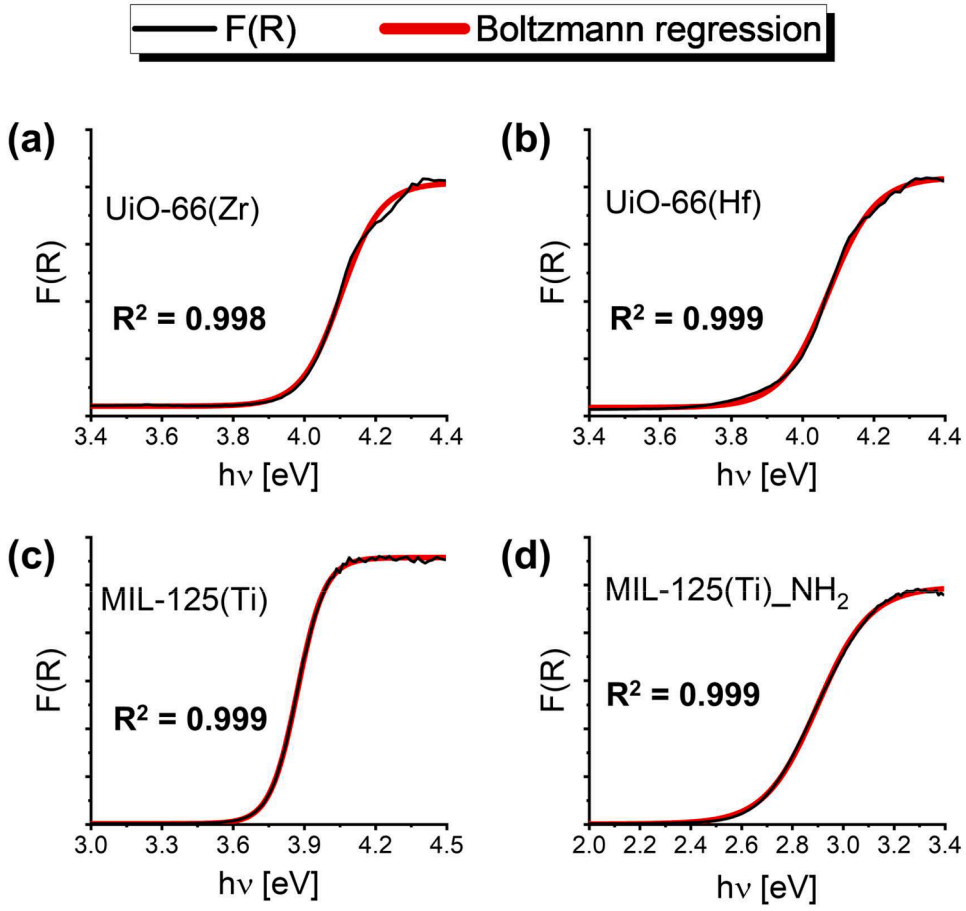

Fig. 7. Optical band gap energies calculated using the Boltzmann regression according to the Eq. (8) by means of the Kubelka-Munk data for (a) UiO-66(Zr), (b) UiO-66(Hf), (c) MIL-125(Ti), and (d) MIL-125(Ti)_NH_2. The black lines represent the F(R) data and the red lines are the Boltzmann regression.

can increase the value of the VBM by adding energy states in the conduction band of UiO-66, which are related to oxygen atoms [88]. However, this effect is not observed in UiO-67_NH_2 because the amino group creates mid-gap states that influences the band gap energies, reducing the influence of the metal on the VBM position. This feature was highlighted by Yasin et al. [88] through the plot of the PDOS of the molecular orbitals for UiO-66 and UiO-66_NH_2 considering both zirconium and hafnium metals.

Finally, the MIL-125(Ti) has an indirect Tauc band gap that reduces from 3.67 to 2.53 eV after the amino functionalization (Table 3). This result is comparable to that obtained elsewhere [30] and should be related to the same phenomenon as in the case of functionalizing UiO-6*x* samples ($x = 6$ or 7) with $–NH_2$ groups. Here, it is clear that the direct and indirect Tauc band gaps are quite similar for both MIL-125 ($E_{g(ind)\_MIL\text{-}125(Ti)} = 3.67$ eV, $E_{g(dir)\_MIL\text{-}125(Ti)} = 3.81$ eV) and its amino functionalized version ($E_{g(ind)\_MIL\text{-}125(Ti)\_NH2} = 2.53$ eV, $E_{g(dir)\_MIL\text{-}125(Ti)\_NH2} = 2.80$ eV). Moreover, the E_g value obtained directly from the Kubelka-Munk UV–vis spectrum is in between both these direct and indirect values: 3.75 and 2.69 eV for MIL-125(Ti) and MIL-125(Ti)_NH_2, respectively. For this reason, both values should be acquired and mentioned when describing the electronic structure of such materials, as discussed before [44].

The log*(1/R)* data was also applied to access the band gap energies for the different MOFs and the results demonstrate linear regions in which the E_g values can be properly extracted (Fig. S9). However, the obtained results seem to be less accurate when compared to those reported in the literature for all MOFs samples (Table S5) [30,87,89,90,93–95]. This can be ascribed to the fact that most works dealing with powdered samples use the Kubelka-Munk model to acquire the UV–vis spectra that is further analyzed to obtain the band gap of the samples. Also, it is clear that the edges of the absorption bands are better defined using the K-M approach than the log*(1/R)* data (Figs. 4 and S7), which can be another source of error.

3.4. Band gap evaluation: the Boltzmann regression

A more recent method for assessing the band gap of semiconductor materials was proposed by Zanatta [34], which evaluated the reliability of the sigmoid-Boltzmann function represented in Eq. (8) by fitting collected data from the $\alpha_{PV}(E)$ spectra (Table 1). Here, α_{max} and α_{min} are the maximum and minimum absorption coefficients, E_0^{Boltz} is the energy coordinate (abscissa axis) in which the absorption coefficient is in halfway between α_{max} and α_{min}, and δE is related to the slope of the sigmoid curve.

$$a(E) = \alpha_{max} + \frac{\alpha_{min} - \alpha_{max}}{1 + exp\left(\frac{E - E_0^{Boltz}}{\delta E}\right)} \tag{8}$$

It was suggested that the E_0^{Boltz} value can be understood as a central energy around which most optical transitions take place (depending on the nature of the band gaps and on the presence of disorders) [34]. For such reason, the band gap energy values should be presented by a Gaussian-like distribution with average energy E_0^{Boltz}, standard deviation ∂E, and Boltzmann factor n_{type}, according to Eq. (9). n_{type} is obtained from the histogram corresponding to an extensive data collection considering standard deviations of 0.1 or 0.2 and is highly influenced by the type of transition exhibited by the material [34].

Table 4
Band gap energies (eV) calculated from Eq. (9) considering the E_0^{Boltz} values obtained from the K-M function and using $n_{dir}^{Boltz} \approx 0.9$ and $n_{ind}^{Boltz} \approx 3.5$.

Method	UiO-66				UiO-67_NH_2			MIL-125	
	Zr	Hf	Zr/Ti	Hf/Ti	Zr	Zr/Hf	Hf	H	NH_2
E_0^{Boltz}	4.11	4.07	4.18	4.49	2.99	2.98	3.01	3.87	2.90
δ_E	0.056	0.067	0.171	0.215	0.111	0.061	0.065	0.058	0.103
$E_{g(dir)}^{Boltz}$	4.06	4.01	4.03	4.30	2.89	2.93	2.95	3.82	2.81
$E_{g(ind)}^{Boltz}$	3.91	3.84	3.58	3.74	2.61	2.77	2.78	3.67	2.54

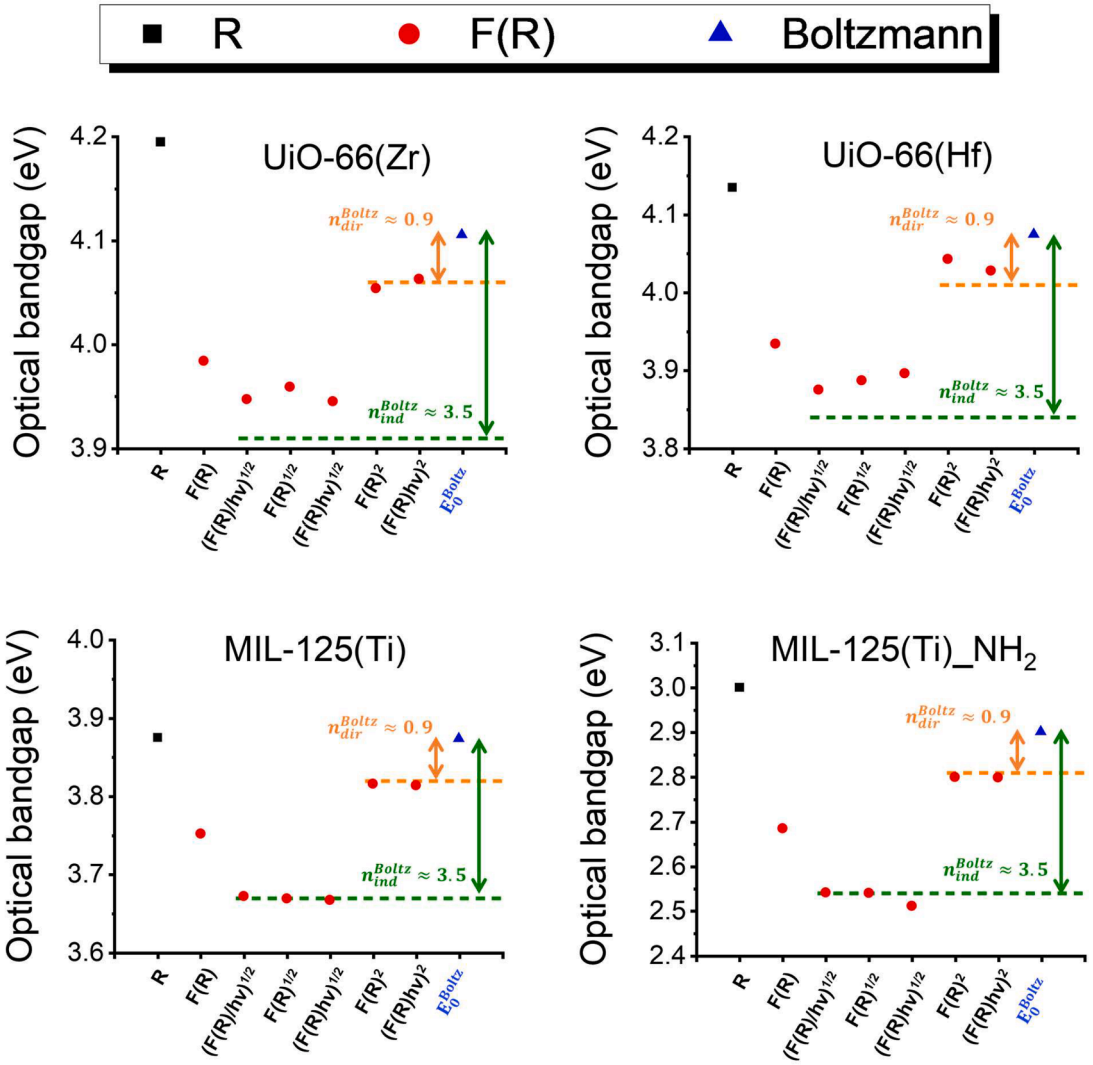

Fig. 8. Optical band gap energies obtained using different methods: extrapolation of the reflectance curve (R), extrapolation of the Kubelka-Munk curve F(R), Cody's band gap [$(F(R)/h\nu)^{1/2}$], indirect band gap [$(F(R)^{1/2}$], Tauc indirect band gap [$(F(R)h\nu)^{1/2}$], direct band gap [$F(R)^2$], Tauc direct band gap [$(F(R)h\nu)^2$], and Boltzmann fit of the F(R) spectra [E_0^{Boltz}]. The horizontal lines represent values obtained for the $E_{g(dir)}^{Boltz}$ (orange) and for the $E_{g(ind)}^{Boltz}$ (green) when considering $n_{dir}^{Boltz} = 0.9$ and $n_{ind}^{Boltz} = 3.5$, respectively. The vertical arrows represent the distance between E_0^{Boltz} and $E_{g(dir)}^{Boltz}$ (orange) and $E_{g(ind)}^{Boltz}$ (green).

$$E_g^{Boltz} = E_0^{Boltz} - n_{type} \times \partial E \quad (9)$$

Following this reasoning, the fitting of the Boltzmann function was applied to the Kubelka-Munk (Figs. 7 and S10) and also to the $\log(1/R)$ data (Fig. S11) of the different compounds synthesized in this work. When using the Kubelka-Munk function, the obtained correlation coefficients (R^2) values for the Boltzmann regression are all above 0.99, showing the good agreement between the experimental K-M data and the empirical method. However, the fit of the Boltzmann regression for the $\log(1/R)$ data exhibited lower coefficient of determination for most compounds, which is ascribed to the inferior accuracy of this approach when dealing with diffuse reflectance UV–vis data.

After fitting the diffuse reflectance UV–vis data to the Boltzmann function, the E_0^{Boltz} was obtained for each compound considering the Kubelka-Munk function (Table 4) and the $\log(1/R)$ data (Table S6). In its original work, Zanatta [34] verified that the value obtained for E_0^{Boltz} is independent of the applied methodology for assessing the absorption coefficient $\alpha(E)$ – i.e., $\alpha_{BLB}(E)$, $\alpha_P(E)$, $\alpha_{PV}(E)$ – revealing that it should be also unaffected to measurements or data treatment details such as improper different spectra correction, for example. This result was found

to be inaccurate in the case of MOFs, as the E_0^{Boltz} values obtained from the Kubelka-Munk differ from those found using the log(*1/R*) approach (Tables 4 and S6).

The band gap energies obtained by the different methods can be separated into groups with similar values depending on the type of the transition (Figs. 8, S12, and S13). Note that the energies obtained by the Cody band gap were always situated in the indirect band gap region, and the raw diffuse reflectance data (*R*) overestimated the E_g values in most cases. Also, the direct and indirect band gaps are closer in the case of UiO-67_NH_2 when comparing to the other compounds. The E_0^{Boltz} energies evaluated using the K-M data were also overestimated and are closer to the direct band gap energies for all the compounds, as demonstrated in Fig. 8. This parameter was also preserved for most of the compounds when using the log*(1/R)* data with the exception of the UiO-67_NH_2 materials (Fig. S13). This is ascribed to the worse fit of the Boltzmann function, as verified by the inferior correlation coefficient in these cases (Fig. S11). Finally, in order to verify if the gap in these MOF systems can be evaluated similarly to other semiconductors as proposed by Zanatta [34], $E_{g(dir)}^{Boltz}$ and $E_{g(ind)}^{Boltz}$ were calculated according to the Eq. (9). The empiric n^{Boltz} values were obtained from a large data collection considering powdered samples with direct ($n_{dir}^{Boltz} \approx 0.9$) and indirect ($n_{ind}^{Boltz} \approx 3.5$) band gaps [34]. The δ_E values were extracted from the fitting of the Boltzmann function to the experimental data, and the obtained values are displayed in Tables 4 and S6.

When analyzing the calculated $E_{g(dir)}^{Boltz}$ and $E_{g(ind)}^{Boltz}$ and comparing them to the other methods, four different scenarios were identified. In the first scenario, there is a match only between the $E_{g(dir)}^{Boltz}$ values and the direct band gaps – i.e., UiO-66(Zr), UiO-66(Hf), and UiO-66(Zr/Ti). In the second case, only the $E_{g(ind)}^{Boltz}$ corresponds to the experimental values, as for the UiO-66(Hf/Ti) material. In the third situation, none of the groups matches the Boltzmann regression, but the $E_{g(dir)}^{Boltz}$ lies in between the two regions (direct and indirect), as observed for the entire UiO-67_NH_2 series (Fig. S12). Finally, for MIL-125(Ti) and MIL-125(Ti)_NH_2 compounds, both the $E_{g(dir)}^{Boltz}$ and $E_{g(ind)}^{Boltz}$ are close to the direct and indirect band gap regions, respectively. These different behaviors provide first evidence for determining the type of optical transition exhibited by the material.

For instance, in the case of the UiO-66(Zr) and UiO-66(Hf), the proximity of the $E_{g(dir)}^{Boltz}$ energies to those obtained by using the $F(R)^2$ and $(F(R)h\nu)^2$ plots (Fig. 8) supports the statement that UiO-66(M) (M = Zr or Hf) has a direct band gap, which is consistent with other reports and computational simulations [79,87]. Then, after introducing titanium, the values acquired for the UiO-66(Zr/Ti) direct band gap follow better the Boltzmann regression (Fig. 8), even though the indirect values are closer to that reported in the literature [87]. This discrepancy is ascribed to the use of the Tauc plot (with different n coefficients: $n = 2$ or $n = ½$) without a previous consideration of the band gap transition type, which highlights the importance of obtaining such information from experimental data. On the other hand, the presence of titanium in UiO-66 (Hf/Ti) seems to modify the type of band gap observed for the UiO-66 materials from direct to indirect. In fact, there is a better agreement between the $E_{g(ind)}^{Boltz}$ and the $(F(R)h\nu)^{1/2}$ plot for this compound, inferring that the Ti-doping can alter the band gap type observed for the UiO-66 materials from direct to indirect in some cases, as mentioned before [89, 90]. Similarly, when considering the UiO-67_NH_2 compounds, the $E_{g(dir)}^{Boltz}$ was found to be closer to the values obtained for direct band gaps (Fig. S12), which is also a signal that these materials exhibit direct electronic transition upon excitation. Finally, for MIL-125(Ti) and MIL-125(Ti)_NH_2, both $E_{g(dir)}^{Boltz}$ and $E_{g(ind)}^{Boltz}$ agree with the energies obtained from other methods. MIL-125(Ti) exhibited an $E_{g(dir)}^{Boltz} = 3.85$ eV that compares to $E_{g(dir)}^{Tauc} = 3.81$ eV, and $E_{g(ind)}^{Boltz} = 3.62$ eV comparing to $E_{g(ind)}^{Tauc} = 3.67$ eV; whereas MIL-125(Ti)_NH_2 presented an $E_{g(dir)}^{Boltz} = 2.87$ eV while $E_{g(dir)}^{Tauc} = 2.80$ eV, and $E_{g(ind)}^{Boltz} = 2.46$ eV while $E_{g(ind)}^{Tauc} = 2.53$ eV. Therefore, it is not possible to infer whether these materials present a direct or indirect band gap based only on the energies obtained by the Boltzmann regression, which accentuates the necessity to acquire both values in this case.

3.5. Band gap evaluation: complex dielectric function and the Kramers-Kronig transformation

The band gap assessment by the different methods presented above (Tauc, Cody, and Boltzmann) takes into consideration the density of states of the material [96,97] and relies on some assumptions. For instance, the Cody band gap considers that the dipole elements in the optical matrix are independent of the photon energy [51]. On the other hand, the Tauc model considers that the momentum is independent of the photon energy in the adsorption edge [98]. However, there is another method named Kramers-Kronig transformation that uses a dielectric transformation, where the optical constants – refractive index (n), extinction coefficient (κ), and reflectivity (R) – are expressed as functions of the real and imaginary parts of the complex dielectric function (ε), as represented in Eq. (10) [99].

$$\varepsilon_{complex} = \varepsilon_{real} - i\varepsilon_{imaginary} \tag{10}$$

In this case, because the bulk material is spatially independent, it is possible to compare the values obtained to those of classical dipole oscillator models [98,100]. In fact, several attempts to correlate empirical data between band gap energies and resonance frequency of oscillators can be found in the literature [101,102]. For instance, Moss [102] related the refractive index to the band gap energy and was able to fit an empirical law for an enormous range of materials. Other variations of the model were also discussed in the literature, as it is the case of the Ravindra and Reddy's relationships [103]. In this case, a relationship between the band gap and the refractive index was proposed for semiconductors. It can also be mentioned the atomic approach of Moss [102], the nearly free electron model of Penn [104], the oscillator concept of Wemple [105], and the optical polarizability approach of Finkenrath [101]. Finally, Hervé and Vandamme [100] further expanded the Penn model based on covalent and ionic bonds within the semiconductor material, creating a mathematical basis for the above mentioned models.

The real and imaginary parts of the dielectric function allow the determination of the macroscopic optical parameters (such as reflectivity, absorption coefficient, refractive index, and penetration depth) [112]. For instance, the real and imaginary parts of the dielectric function can be related to the extinction coefficient (κ) and the refractive index (n), which are functions of the frequency ν – according to the Eqs. (11) and (12).

$$\varepsilon_{real} = n(\nu)^2 - \kappa(\nu)^2 \tag{11}$$

$$\varepsilon_{imaginary} = 2n(\nu)\kappa(\nu) \tag{12}$$

In order to describe the spatial independence, the complex transformation of the dielectric function is conducted in a polar coordinate system. It is then possible to express the Penn model with only two parameters with spatial independence (i.e. an infinite inhomogeneous medium), as in Eq. (13) [106].

$$\Phi = tan^{-1}\left(\frac{\varepsilon_{imaginary}}{\varepsilon_{real}}\right) = tan^{-1}\left(\frac{2n(\nu)\kappa(\nu)}{n(\nu)^2 - \kappa(\nu)^2}\right) \tag{13}$$

The Kramers–Kronig [107,108] transformation (K-K transformation) is of an extremely importance, as it can be used to obtain the extinction coefficient (κ) and the refractive index (n) of the material through diffuse reflectance spectra, as highlighted in Eqs. (14) and (15) [109], where, R is the diffuse reflectance data (normalized from 0 to 1).

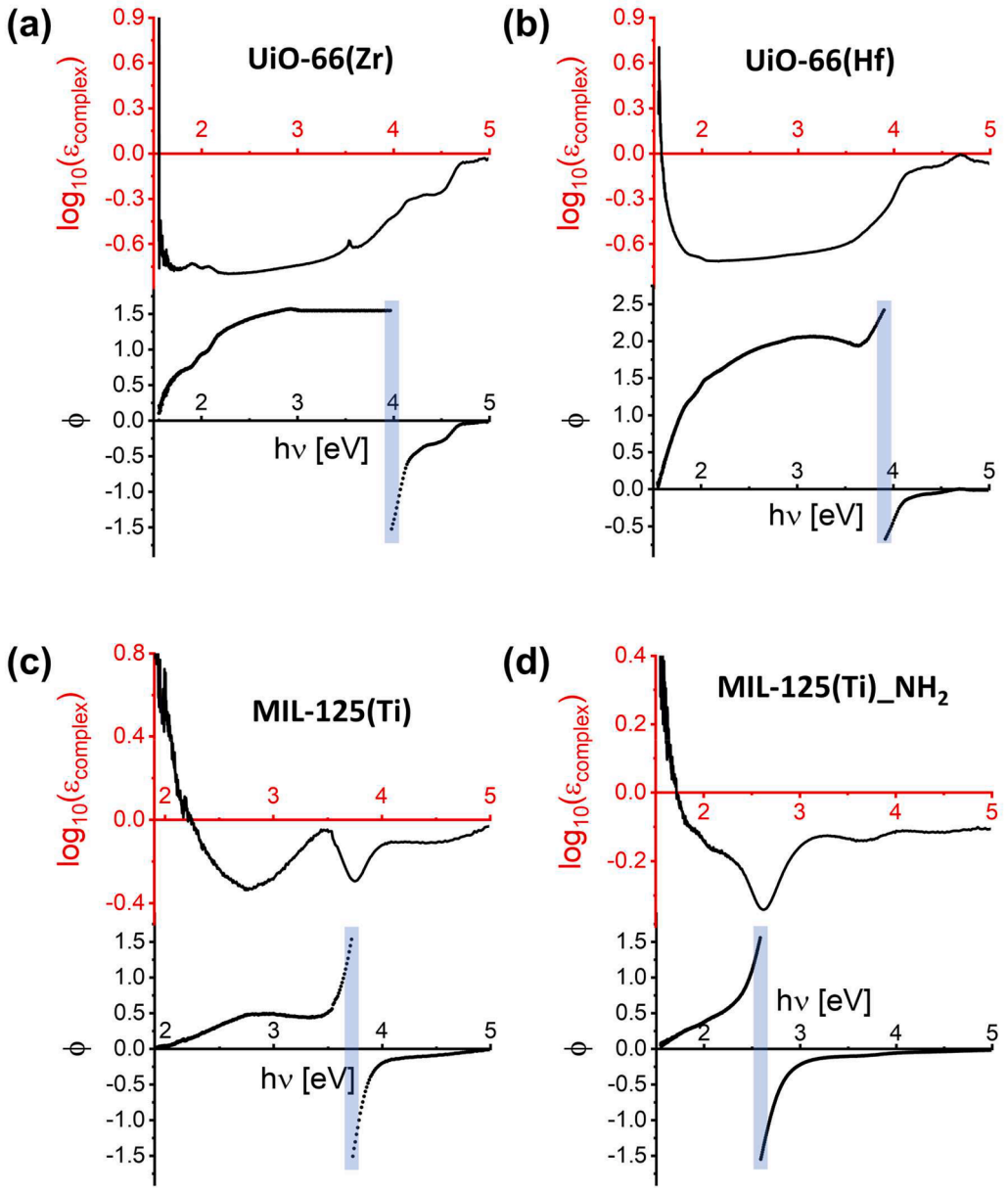

Fig. 9. Dispersion-dissipation versus energy plots for (a) UiO-66(Zr), (b) UiO-66(Hf), (c) MIL-125(Ti), and (d) MIL-125(Ti)_NH_2. The absorption edge corresponding to the discontinuity at $\Phi \rightarrow 90^{\circ}$ is represented as a blue region.

$$n(\nu) = \frac{1 - R(\nu)}{1 + R(\nu) - 2cos\theta(\nu)\sqrt{R(\nu)}} \tag{14}$$

$$\kappa(\nu) = \frac{-2sin\theta(\nu)\sqrt{R(\nu)}}{1 + R(\nu) - 2cos\theta(\nu)\sqrt{R(\nu)}} \tag{15}$$

The inovation in using the K-K aproach lies in the fact that the real and imaginary parts of the complex reflectance are related via causality and therefore, the unknown phase shift angle can be obtained using the Hilbert transform. In summary, the Kramers-Kronig relations are a general property of response functions that can be traced back to the causality principle [107,108]. The imaginary part of a response function describes how a system dissipates energy, since it is in phase with the driving force. The Kramers–Kronig relations imply that observing the dissipative response of a system is sufficient to determine its out of phase (reactive) response, and vice versa. In this case, the phase shift angle of the sample (θ) is given by Eq. (16), where ν_m is the medium frequency on the range of the collected spectra [109].

$$\theta(\nu) = \frac{2\nu_m}{\pi} \int_0^{\infty} \frac{ln\sqrt{R(\nu)}}{\nu^2 - \nu_m^2} d\nu \tag{16}$$

The dispersion-dissipation – $\log(\varepsilon_{complex})$ and Φ – plotted against the photon energy ($h\nu$) characterises the optical properties of the material since $n(\nu) - \kappa(\nu) \rightarrow 0$ in the region where $\Phi \rightarrow -\pi/2$ [109]. In fact, for semiconductor materials, the Φ vs ($h\nu$) plot exhibits a discontinuity and a 180° phase shift when $\Phi \rightarrow 90^{\circ}$ [109]. This effect was attributed to a polarization effect in semiconductors and insulators [110]. The discontinuity observed in the Φ vs ($h\nu$) plot for the MOF materials (Figs. 9 and S14) confirms therefore their semiconductor character.

Finally, combining Eqs. (11) to (16) and the Tauc method (Eq. (6)), Eq. (17) can be derived, which relates the band gap energies (E_g) to the refractive index $n(\nu)$ and to the photon energy $h\nu$, where μ_0 is the vacuum permeability [109].

$$(h\nu)^{-1} = -\mu_0 n(\nu)^2 + (E_g)^{-1} \tag{17}$$

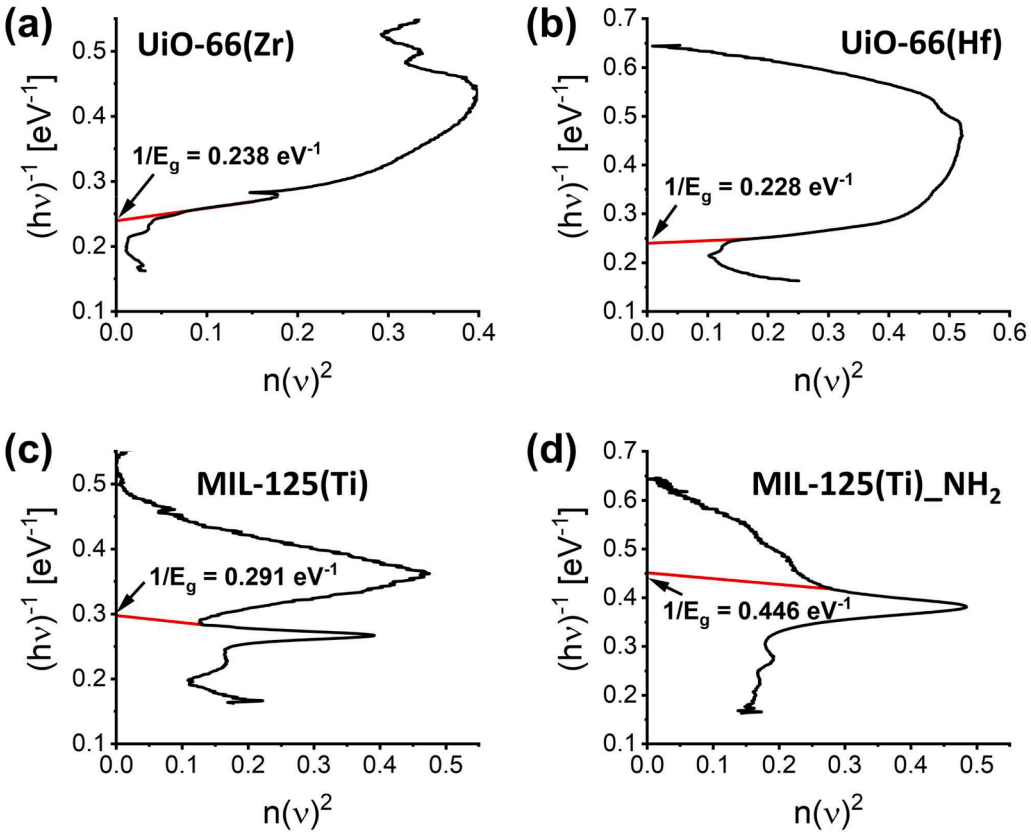

Fig. 10. Band gap energies calculated for (a) UiO-66(Zr), (b) UiO-66(Hf), (c) MIL-125(Ti), and (d) MIL-125(Ti)_NH_2 compounds by using the Kramers-Kronig transformation through the plot of $(h\nu)^{-1}$ versus $n(\nu)^2$. The red line highlights the position where the E_g^{-1} values were assessed. This line has a positive slope for direct band gaps and a negative slope for indirect band gaps.

Table 5
Band gap energies calculated using the Kramers-Kronig transformation, comparison with the average for direct and indirect values $\overline{E_g}$, and percentage of error between E_g^{K-K} and $\overline{E_g}$.

MOF	E_g^{K-K}	$\overline{E_g}$		$\lvert\frac{E_g^{K-K}-\overline{E_g}}{\overline{E_g}}\rvert$	
		Direct	Indirect	$\overline{E_g}$ direct	$\overline{E_g}$ indirect
	[eV]	[eV]	[eV]	[%]	[%]
UiO-66(Zr)	4.20	4.07	3.94	**3.2**	6.6
UiO-66(Hf)	4.39	4.04	3.86	**8.6**	13.7
UiO-66(Zr/Ti)	4.35	4.05	3.69	**7.4**	17.9
UiO-66(Hf/Ti)	4.41	4.17	3.73	**5.8**	18.2
UiO-67(Zr)_NH_2	3.22	2.93	2.76	**9.9**	16.7
UiO-67(Zr/Hf)_NH_2	3.13	2.96	2.86	**5.7**	9.4
UiO-67(Hf)_NH_2	3.13	2.98	2.87	**5.0**	9.1
MIL-125(Ti)	3.44	3.83	3.66	10.2	**6.0**
MIL-125(Ti)_NH_2	2.24	2.82	2.51	20.6	**10.8**

* direct values were obtained considering the average between the Tauc direct, the pure direct, and the Boltzmann direct band gaps. Indirect values were obtained considering the average between the Cody, Tauc indirect, pure indirect, and Boltzmann indirect band gaps.

A plot of $(h\nu)^{-1}$ (the inverse of the photon energy [eV^{-1}]) in the *y*-axis versus $n(\nu)^2$ on the *x*-axis makes explicit a linear regime region which denotates the onset of absorption [109]. The extrapolation of this curve into the *y*-axis corresponds to the inverse of the band gap energy of the material $(E_g)^{-1}$ (Fig. 10). The band gap values obtained through the K-K transformation (E_g^{K-K}) are shown in Table 5, alongside the average values for the direct (Tauc direct, Boltzmann direct, and pure direct) and indirect (Tauc indirect, Cody, Boltzmann indirect, and pure indirect) methods, and an error between the E_g^{K-K} and each band gap type (direct or indirect).

Interesting information can be obtained when analyzing the band gap and the error values between the band gap energies obtained using the K-K transform and the average value from Tauc, Cody, and Boltzmann methods. First, the Kramers-Kronig approach overestimates the optical band gap for most compounds, except for MIL-125(Ti) and MIL-125(Ti)_NH_2. In addition, the discrepancies observed are closely related to the type of transition, as E_g^{K-K} and $\overline{E_g}$ can vary by up to an order of magnitude considering the same sample. In general, the E_g^{K-K} energies obtained for the UiO-6*x* series were closer to the average values of direct transitions, suggesting that this family of materials exhibits a direct band gap, in agreement with the Boltzmann regression results (Figs. 8, S12, and S13). However, UiO-66(Hf/Ti) is an exception. It appears to exhibit an indirect band gap when considering the proximity of the $E_{g(ind)}^{Boltz}$ but is closer to the direct average when considering the E_g^{K-K} (Tables 3–5). Finally, MIL-125(Ti) and MIL-125(Ti)_NH_2 shows a smaller error for the indirect band gap, indicating that this type of transition is favored in these materials. In contrast, using the Boltzmann regression, both direct and indirect band gaps assumptions are reasonable for these two materials.

It is worth mentioning that the use of the complex dielectric function to assess band gap energies of semiconductors must be applied carefully. In fact, since the method considers the inverse plot of energy ($1/E_g$ against $n(\nu)^2$) any variation in the position of the interception line can impact enormously the results – i.e.: for $1/E_g = 0.40$ eV^{-1} → $E_g = 2.50$ eV; whereas $1/E_g = 0.43$ eV^{-1} → $E_g = 2.33$ eV. Moreover, there are several different regions that present a linear behavior when plotting $1/E_g$ against $n(\nu)^2$ (Figs. 10 and S15). Therefore, there are several places where the tangent connecting the curve to the *y*-axis can be plotted (as in

Table 6
Optical band gap transitions attributions (direct or indirect) considering the average energy values calculated from the Kubelka-Munk transformed UV–vis spectra. Direct transitions considered for the average: "pure" direct and Tauc direct. Indirect transitions considered for the average: "pure" indirect, Tauc indirect, and Cody band gap. The values were compared to the energies calculated using the Boltzmann regression ($E_{g(dir)}^{Boltz}$ and $E_{g(ind)}^{Boltz}$) and the Kramers-Kronig (E_g^{K-K}) transformation.

MOF	$\overline{E_{g(dir)}}$ [eV]	$\overline{E_{g(indir)}}$ [eV]	$E_{g(dir)}^{Boltz}$ [eV]	$E_{g(ind)}^{Boltz}$ [eV]	Boltzmann attribution	E_g^{K-K} [eV]	K-K attribution	Conclusion
UiO-66(Zr)	4.06	3.96	**4.06**	3.91	Direct	4.20	Direct	Direct
UiO-66(Hf)	4.04	3.89	**4.01**	3.84	Direct	4.39	Direct	Direct
UiO-66(Zr/Ti)	4.01	3.77	**4.03**	3.58	Direct	4.35	Direct	Direct
UiO-66(Hf/Ti)	4.05	3.78	4.30	**3.74**	Indirect	4.41	Direct	Inconclusive
UiO-67(Zr)_NH_2	2.93	2.85	**2.89**	2.61	Direct	3.22	Direct	Direct
UiO-67(Zr/Hf)_NH_2	2.96	2.91	**2.93**	2.77	Direct	3.13	Direct	Direct
UiO-67(Hf)_NH_2	2.98	2.91	**2.95**	2.78	Direct	3.13	Direct	Direct
MIL-125(Ti)	3.82	3.67	**3.82**	**3.67**	Direct/indirect	3.44	Indirect	Indirect
MIL-125(Ti)_NH_2	2.80	2.53	**2.81**	**2.54**	Direct/indirect	2.24	Indirect	Indirect

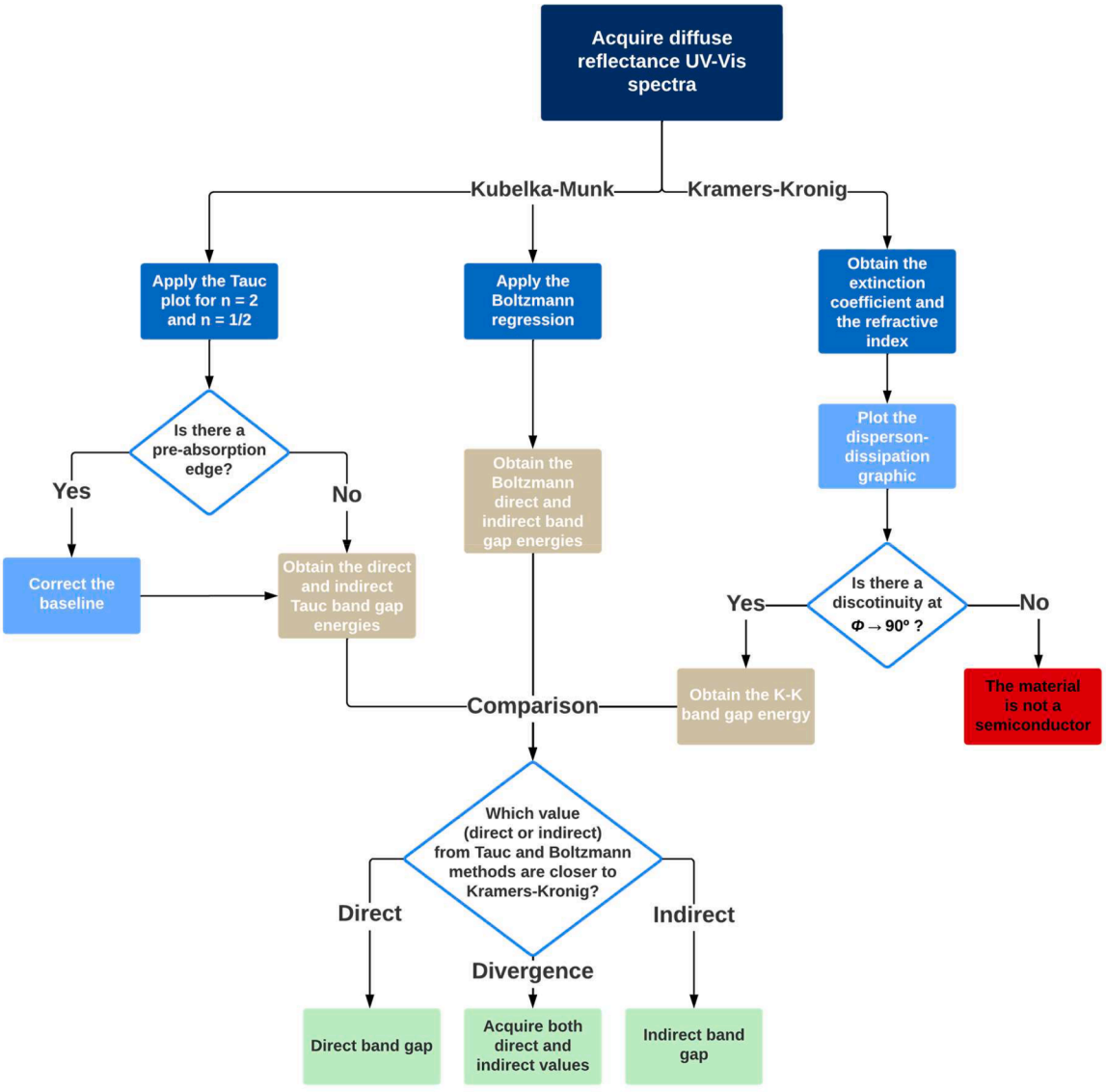

Fig. 11. Flowchart demonstrating the methodology for determining whether a material has a direct or indirect band gap transition.

the Tauc plot for the tangent extrapolated to the *x*-axis, as discussed above), potentially favoring enormous error in the E_g determination using the K-K transform. Nevertheless, the method is very attractive to confirm the band gap type for different materials. It can confirm results obtained from other methods, such as the Tauc plot (direct and indirect), the Cody (indirect), the pure direct, and the pure indirect approaches.

Finally, the average energy grouping the regions of direct (pure direct, and Tauc direct) and indirect (pure indirect, Tauc indirect, and Cody band gap) transitions were calculated using the Kubelka-Munk model and were compared to other methods (Boltzmann and Kramers-Kronig) for determining the optical band gap type of MOF materials (Table 6). Both Boltzmann and Kramers-Kronig attributions converge for

most materials. In fact, the entire UiO-6*x* series is found to present direct band gap transitions, with the exception of UiO-66(Hf/Ti), where the analysis was inconclusive (Boltzmann: indirect; K-K: direct). In contrast, both transition types were assigned to MIL-125(Ti) and MIL-125(Ti)_NH_2 considering the Boltzmann regression, while the Kramers-Kronig model was closer to the average energies of the indirect optical band gap. Therefore, these materials are assumed to exhibit indirect transitions. In addition, note that the tangent line connecting the $(h\nu)^{-1}$ curve to the *y*-axis in the Kramers-Kronig plot has a negative slope for MIL-125 (Ti) and MIL-125(Ti)_NH_2 (Fig. 10). This slope is positive for all the other MOF compounds, indicating that it can also be a tool for determining the band gap transition type: for positive slopes, the band gap is direct; for negative slopes, the band gap is indirect.

To sum it up, a complete methodology for determining band gap types by using diffuse reflectance UV–vis spectroscopy in powdered semiconductor materials is proposed (Fig. 11).

4. Conclusions

This work evaluated the different methods to access the band gap of powdered and single-crystal MOF materials by means of diffuse reflectance UV–vis data. The results have been extensively compared to the literature. The Kubelka-Munk approach and the log(1/R) were individually considered when treating the diffuse reflectance data. The results demonstrate that, although the Kubelka-Munk method presents some constraints regarding high absorbent samples, it is more suitable than the log(1/R) approach because it provides spectra with sharper absorption edges, which facilitates the further interpretation and characterization of the band gaps. Several methods were applied to obtain the E_g values of the different materials, worth mentioning the band gap obtained directly from the diffuse reflectance data, from the Kubelka-Munk data, from the log(1/R) data, the Cody band gap $[(\alpha/h\nu)^{1/2}]$, the indirect band gap $(\alpha^{1/2})$, the Tauc indirect band gap $[(\alpha h\nu)^{1/2}]$, the direct band gap (α^2), the Tauc direct band gap $[(\alpha h\nu)^2]$, the Boltzmann band gap, and the Kramers-Kronig band gap. These different approaches were compared with both experimental and computational data from the literature and the limitations of some procedures were emphasized. A comparative method was proposed for determining the type of band gap exhibited by the different materials without needing computer simulations. The Boltzmann regression coupled to the Kramers-Kronig transformation offers a solid base for determining either if a material has a direct or an indirect gap by only comparing the obtained E_g^{Boltz} and E_g^{K-K} result with those from the other methodologies (i.e. Tauc direct and indirect band gap). The influence of pre-data treatment and baseline correction were also highlighted in cases where a pre-absorption edge is present, which can lead to a misevaluation of the band gap values. Finally, for some materials such as MIL-125(Ti) and MIL-125(Ti)_NH_2, the need of acquiring both the indirect and direct band gap values was also discussed. This work highlights how delicate is determining the nature of the band gap and its value by using UV–vis spectroscopy, which explains the scatter of results in the literature. This study should also contribute to determine band gaps more accurately, leading to more reliability in different areas of chemistry, physics, and materials engineering where these gaps are of importance.

CRediT authorship contribution statement

Pedro H.M. Andrade: Conceptualization, Methodology, Formal analysis, Investigation, Data curation, Visualization, Writing – original draft. **Christophe Volkringer:** Writing – review & editing, Visualization, Validation, Supervision, Project administration, Funding acquisition. **Thierry Loiseau:** Writing – review & editing, Visualization, Validation, Supervision, Project administration, Funding acquisition. **Antonio Tejeda:** Writing – review & editing, Visualization, Validation. **Matthieu Hureau:** Writing – review & editing, Visualization, Validation, Supervision, Resources, Project administration, Funding acquisition. **Alain Moissette:** Writing – review & editing, Visualization, Validation, Supervision, Resources, Project administration, Funding acquisition.

Declaration of competing interest

The authors declare that they have no known competing financial interests or personal relationships that could have appeared to influence the work reported in this paper.

Data availability

Data will be made available on request.

Acknowledgements

The “Fonds Européen de Développement Régional” (FEDER), the “Centre National de la Recherche Scientifique” (CNRS), the “Région Hauts de France”, and the “Ministère de l’Education Nationale de l’Enseignement Supérieur et de la Recherche” are acknowledged for the funding of X-ray diffractometers from the Chevreul Institute platform. Dr. Sylvain Duval is recognized for its valuable contribution to the liquid ^{1}H NMR analysis. P. H. M. A. would like to thank the University of Lille for the PhD grant.

References

[1] A. Fujishima, K. Honda, Electrochemical photolysis of water at a semiconductor electrode, Nature 238 (1972) 37–38, https://doi.org/10.1038/238037a0.
[2] M.A. Fox, M.T. Dulay, Heterogeneous photocatalysis, Chem. Rev. 93 (1993) 341–357, https://doi.org/10.1021/cr00017a016.
[3] A. Chatterjee, L. Wang, P. Van Der Voort, Metal–organic frameworks in photocatalytic Z-scheme heterojunctions: an emerging technology, Chem. Commun. 59 (2023) 3627–3654, https://doi.org/10.1039/D2CC05819G.
[4] F. Fischer, Photoelectrode, photovoltaic and photosynthetic microbial fuel cells, Renew. Sustain. Energy Rev. 90 (2018) 16–27, https://doi.org/10.1016/j.rser.2018.03.053.
[5] S. Chu, Y. Wang, Y. Guo, J. Feng, C. Wang, W. Luo, X. Fan, Z. Zou, Band structure engineering of carbon nitride: in search of a polymer photocatalyst with high photooxidation property, ACS Catal. 3 (2013) 912–919, https://doi.org/10.1021/cs4000624.
[6] L. Jiao, Y. Wang, H.L. Jiang, Q. Xu, Metal–organic frameworks as platforms for catalytic applications, Adv. Mater. 30 (2018) 1–23, https://doi.org/10.1002/adma.201703663.
[7] P.H.M. Andrade, A.L.M. Gomes, H.G. Palhares, C. Volkringer, Post-synthetic modification of aluminum trimesate and copper trimesate with TiO2 nanoparticles for photocatalytic applications, J. Mater. Sci. 57 (2022) 4481–4503, https://doi.org/10.1007/s10853-021-06842-w.
[8] M.R. Hoffmann, S.T. Martin, W. Choi, D.W. Bahnemann, Environmental applications of semiconductor photocatalysis, Chem. Rev. 95 (1995) 69–96, https://doi.org/10.1021/cr00033a004.
[9] X. Deng, Z. Li, H. García, Visible light induced organic transformations using metal-organic-frameworks (MOFs), Chem. Eur. J. 23 (2017) 11189–11209, https://doi.org/10.1002/chem.201701460.
[10] R. Asahi, T. Morikawa, T. Ohwaki, K. Aoki, Y. Taga, Visible-light photocatalysis in nitrogen-doped titanium oxides, Science 293 (2001) 269–271, https://doi.org/10.1126/science.1061051 (80.).
[11] C.W. Jones, Metal–organic frameworks and covalent organic frameworks: emerging advances and applications, JACS Au 2 (2022) 1504–1505, https://doi.org/10.1021/jacsau.2c00376.
[12] S.M. Moosavi, A. Nandy, K.M. Jablonka, D. Ongari, J.P. Janet, P.G. Boyd, Y. Lee, B. Smit, H.J. Kulik, Understanding the diversity of the metal-organic framework ecosystem, Nat. Commun. 11 (2020) 1–10, https://doi.org/10.1038/s41467-020-17755-8.
[13] J.L. Mancuso, A.M. Mroz, K.N. Le, C.H. Hendon, Electronic structure modeling of metal-organic frameworks, Chem. Rev. 120 (2020) 8641–8715, https://doi.org/10.1021/acs.chemrev.0c00148.
[14] N. Kolobov, M.G. Goesten, J. Gascon, Metal–organic frameworks: molecules or semiconductors in photocatalysis? Angew. Chem. Int. Ed. 60 (2021) 26038–26052, https://doi.org/10.1002/anie.202106342.
[15] S. Wang, L. Pan, J.J. Song, W. Mi, J.J. Zou, L. Wang, X. Zhang, Titanium-defected undoped anatase TiO2 with p-type conductivity, room-temperature ferromagnetism, and remarkable photocatalytic performance, J. Am. Chem. Soc. 137 (2015) 2975–2983, https://doi.org/10.1021/ja512047k.

[16] J.P. Kleider, Y.M. Soro, R. Chouffot, A.S. Gudovskikh, P. Roca i Cabarrocas, J. Damon-Lacoste, D. Eon, P.J. Ribeyron, High interfacial conductivity at amorphous silicon/crystalline silicon heterojunctions, J. Non-Cryst. Solids 354 (2008) 2641–2645, https://doi.org/10.1016/j.jnoncrysol.2007.09.087.

[17] K. Lu, D. Erb, M. Liu, Thermal stability and electrical conductivity of carbon-enriched silicon oxycarbide, J. Mater. Chem. C. 4 (2016) 1829–1837, https://doi.org/10.1039/c6tc00069j.

[18] V. Somjit, P. Thinsoongnoen, S. Waiprasoet, T. Pila, P. Pattanasattayavong, S. Horike, K. Kongpatpanich, Processable UiO-66 metal–organic framework fluid gel and electrical conductivity of its nanofilm with sub-100 nm thickness, ACS Appl. Mater. Interfaces 13 (2021) 30844–30852, https://doi.org/10.1021/acsami.1c07262.

[19] P. Salcedo-Abraira, A. Santiago-Portillo, P. Atienzar, P. Bordet, F. Salles, N. Guillou, E. Elkaim, H. Garcia, S. Navalon, P. Horcajada, A highly conductive nanostructured PEDOT polymer confined into the mesoporous MIL-100(Fe), Dalton Trans. 48 (2019) 9807–9817, https://doi.org/10.1039/C9DT00917E.

[20] P.H.M. Andrade, H. Palhares, C. Volkringer, T. Loiseau, M. Hureau, E. Nunes, A. Moissette, State of the art in visible-light photocatalysis of aqueous pollutants using metal-organic frameworks, J. Photochem. Photobiol. C Photochem. Rev. 57 (2023) 100635, https://doi.org/10.1016/j.jphotochemrev.2023.100635.

[21] L.D. Yuan, H.X. Deng, S.S. Li, S.H. Wei, J.W. Luo, Unified theory of direct or indirect band-gap nature of conventional semiconductors, Phys. Rev. B 98 (2018) 1–10, https://doi.org/10.1103/PhysRevB.98.245203.

[22] X. Guo, L. Liu, Y. Xiao, Y. Qi, C. Duan, F. Zhang, Band gap engineering of metal-organic frameworks for solar fuel productions, Coord. Chem. Rev. 435 (2021), https://doi.org/10.1016/j.ccr.2021.213785.

[23] R. Elzein, C.M. Chang, I. Ponomareva, W.Y. Gao, S. Ma, R. Schlaf, Advanced photoemission spectroscopy investigations correlated with DFT calculations on the self-assembly of 2D metal organic frameworks nano thin films, ACS Appl. Mater. Interfaces 8 (2016) 31403–31412, https://doi.org/10.1021/acsami.6b10340.

[24] A.H. Wilson, The theory of electronic semi-conductors, Proc. R. Soc. Lond. Ser. A Math. Phys. Sci. 133 (1931) 458–491, https://doi.org/10.1098/rspa.1931.0162.

[25] A.H. Wilson, The theory of electronic semi-conductors II, Proc. R. Soc. Lond. Ser. A Math. Phys. Sci. 134 (1931) 277–287, https://doi.org/10.1098/rspa.1931.0196.

[26] C.A. Mead, W.G. Spitzer, Fermi level position at semiconductor surfaces, Phys. Rev. Lett. 10 (1963) 471–472, https://doi.org/10.1103/PhysRevLett.10.471.

[27] Z. Huang, M. Lee Tang, Semiconductor nanocrystal light absorbers for photon upconversion, J. Phys. Chem. Lett. 9 (2018) 6198–6206, https://doi.org/10.1021/acs.jpclett.8b02154.

[28] C. Dette, M.A. Pérez-Osorio, C.S. Kley, P. Punke, C.E. Patrick, P. Jacobson, F. Giustino, S.J. Jung, K. Kern, TiO2 anatase with a bandgap in the visible region, Nano Lett. 14 (2014) 6533–6538, https://doi.org/10.1021/nl503131s.

[29] L.M. Yang, G.Y. Fang, J. Ma, E. Ganz, S.S. Han, Band gap engineering of paradigm MOF-5, Cryst. Growth Des. 14 (2014) 2532–2541, https://doi.org/10.1021/cg500243s.

[30] C.H. Hendon, D. Tiana, M. Fontecave, C. Sanchez, L. D'Arras, C. Sassoye, L. Rozes, C. Mellot-Draznieks, A. Walsh, Engineering the optical response of the titanium-MIL-125 metal-organic framework through ligand functionalization, J. Am. Chem. Soc. 135 (2013) 10942–10945, https://doi.org/10.1021/ja405350u.

[31] L.M. Yang, G.Y. Fang, J. Ma, R. Pushpa, E. Ganz, Halogenated MOF-5 variants show new configuration, tunable band gaps and enhanced optical response in the visible and near infrared, Phys. Chem. Chem. Phys. 18 (2016) 32319–32330, https://doi.org/10.1039/c6cp06981a.

[32] Q. Wang, Q. Gao, A.M. Al-Enizi, A. Nafady, S. Ma, Recent advances in MOF-based photocatalysis: environmental remediation under visible light, Inorg. Chem. Front. 7 (2020) 300–339, https://doi.org/10.1039/c9qi01120j.

[33] C.J.H. Wort, R.S. Balmer, Diamond as an electronic material, Mater. Today 11 (2008) 22–28, https://doi.org/10.1016/S1369-7021(07)70349-8.

[34] A.R. Zanatta, Revisiting the optical bandgap of semiconductors and the proposal of a unified methodology to its determination, Sci. Rep. 9 (2019) 11225, https://doi.org/10.1038/s41598-019-47670-y.

[35] V. Sarritzu, N. Sestu, D. Marongiu, X. Chang, Q. Wang, S. Masi, S. Colella, A. Rizzo, A. Gocalinska, E. Pelucchi, M.L. Mercuri, F. Quochi, M. Saba, A. Mura, G. Bongiovanni, Direct or indirect bandgap in hybrid lead halide perovskites? Adv. Opt. Mater. 6 (2018) 1–8, https://doi.org/10.1002/adom.201701254.

[36] G. Wang, C. Robert, M.M. Glazov, F. Cadiz, E. Courtade, T. Amand, D. Lagarde, T. Taniguchi, K. Watanabe, B. Urbaszek, X. Marie, In-plane propagation of light in transition metal dichalcogenide monolayers: optical selection rules, Phys. Rev. Lett. 119 (2017) 1–7, https://doi.org/10.1103/PhysRevLett.119.047401.

[37] W. Eberhardt, F.J. Himpsel, Dipole selection rules for optical transitions in the fcc and bcc lattices, Phys. Rev. B 21 (1980) 5572–5576, https://doi.org/10.1103/PhysRevB.21.5572.

[38] C. Kittel, Introduction to Solid State Physics, Wiley, 2005, pp. 185–219.

[39] Y.P. Varshni, Band-to-band radiative recombination in groups IV, VI, and III-V semiconductors (I), Phys. Status Solidi 19 (1967) 459–514, https://doi.org/10.1002/pssb.19670190202.

[40] R. Soref, B. Bennett, Electrooptical effects in silicon, IEEE J. Quantum Electron. 23 (1987) 123–129, https://doi.org/10.1109/JQE.1987.1073206.

[41] S. Zwerdling, B. Lax, L.M. Roth, Oscillatory magneto-absorption in semiconductors, Phys. Rev. 108 (1957) 1402–1408, https://doi.org/10.1103/PhysRev.108.1402.

[42] J. Tauc, R. Grigorovici, A. Vancu, Optical properties and electronic structure of amorphous germanium, Phys. Status Solidi 15 (1966) 627–637, https://doi.org/10.1002/pssb.19660150224.

[43] N.F. Mott, E.A. Davis, Conduction in non-crystalline systems V. Conductivity, optical absorption and photoconductivity in amorphous semiconductors, Philos. Mag. 22 (1970) 903–922, https://doi.org/10.1080/14786437008221061.

[44] J.B. Coulter, D.P. Birnie, Assessing tauc plot slope quantification: ZnO thin films as a model system, Phys. Status Solidi Basic Res. 255 (2018) 1–7, https://doi.org/10.1002/pssb.201700393.

[45] Y. Feng, S. Lin, S. Huang, S. Shrestha, G. Conibeer, Can Tauc plot extrapolation be used for direct-band-gap semiconductor nanocrystals? J. Appl. Phys. 117 (2015) https://doi.org/10.1063/1.4916090.

[46] B.D. Viezbicke, S. Patel, B.E. Davis, D.P. Birnie, Evaluation of the Tauc method for optical absorption edge determination: ZnO thin films as a model system, Phys. Status Solidi Basic Res. 252 (2015) 1700–1710, https://doi.org/10.1002/pssb.201552007.

[47] R. López, R. Gómez, Band-gap energy estimation from diffuse reflectance measurements on sol-gel and commercial TiO2: a comparative study, J. Sol-Gel Sci. Technol. 61 (2012) 1–7, https://doi.org/10.1007/s10971-011-2582-9.

[48] A. Dolgonos, T.O. Mason, K.R. Poeppelmeier, Direct optical band gap measurement in polycrystalline semiconductors: a critical look at the Tauc method, J. Solid State Chem. 240 (2016) 43–48, https://doi.org/10.1016/j.jssc.2016.05.010.

[49] M. Meinert, G. Reiss, Electronic structure and optical band gap determination of NiFe2O4, J. Phys. Condens. Matter 26 (2014) 115503, https://doi.org/10.1088/0953-8984/26/11/115503.

[50] P. Makuła, M. Pacia, W. Macyk, How to correctly determine the band gap energy of modified semiconductor photocatalysts based on UV–vis spectra, J. Phys. Chem. Lett. 9 (2018) 6814–6817, https://doi.org/10.1021/acs.jpclett.8b02892.

[51] G.D. Cody, B.G. Brooks, B. Abeles, Optical absorption above the optical gap of amorphous silicon hydride, Sol. Energy Mater. 8 (1982) 231–240, https://doi.org/10.1016/0165-1633(82)90065-X.

[52] P. Bouguer, Traité d'optique sur la gradation de la lumière, Guerin and Delatour, Paris, 1852. https://gallica.bnf.fr/ark:/12148/bpt6k948469/f2.item.

[53] J.H. Lambert, Photometria, Sive de Mensura et Gradibus Luminis, Colorum et Umbrae, Leipzig : W. Engelmann, 1760. https://archive.org/details/lambertsphotome00lambgoog.

[54] Beer, Bestimmung der Absorption des rothen Lichts in farbigen Flüssigkeiten, Ann. Phys. 162 (1852) 78–88, https://doi.org/10.1002/andp.18521620505.

[55] J.I. Pankove, Optical Processes in Semiconductors, Dover Publications, New York, 1971. I. 0-486-60275-3.

[56] R. Vahalová, L. Tichý, M. Vlček, H. Tichá, Far infrared spectra and bonding arrangement in some Ge–Sb–S glasses, Phys. Status Solidi 181 (2000) 199–209, https://doi.org/10.1002/1521-396X(200009), 181:1<199::AID−PSSA199>3.0.CO;2-X.

[57] P. Kubelka, F. Munk, An article on optics of paint layers, Z. Tech. Phys. 12 (1931) 593–601.

[58] Y. Lee, S. Kim, J.K. Kang, S.M. Cohen, Photocatalytic CO2 reduction by a mixed metal (Zr/Ti), mixed ligand metal-organic framework under visible light irradiation, Chem. Commun. 51 (2015) 5735–5738, https://doi.org/10.1039/c5cc00686d.

[59] D. Yamashita, Y. Nakajima, A. Ishizaki, M. Uda, Photoelectron spectrometer equipped with open counter for electronic structures of organic materials, J. Surf. Anal. 14 (2008) 433–436. http://www.sasj.jp/JSA/CONTENTS. /vol.14_4/Vol.14No.4/Vol.14 No.4 433-436.pdf.

[60] R.J. Davis, M.T. Lloyd, S.R. Ferreira, M.J. Bruzek, S.E. Watkins, L. Lindell, P. Sehati, M. Fahlman, J.E. Anthony, J.W.P. Hsu, Determination of energy level alignment at interfaces of hybrid and organic solar cells under ambient environment, J. Mater. Chem. 21 (2011) 1721–1729, https://doi.org/10.1039/C0JM02349C.

[61] J. Jasieniak, M. Califano, S.E. Watkins, Size-dependent valence and conduction band-edge energies of semiconductor nanocrystals, ACS Nano 5 (2011) 5888–5902, https://doi.org/10.1021/nn201681s.

[62] P. Kubelka, New contributions to the optics of intensely light-scattering materials. Part I, J. Opt. Soc. Am. 44 (1948) 330, https://doi.org/10.1364/josa.44.000330.

[63] D.R. Duncan, The colour of pigment mixtures, Proc. Phys. Soc. 52 (1940) 390–401, https://doi.org/10.1088/0959-5309/52/3/310.

[64] T. Burger, J. Kuhn, R. Caps, J. Fricke, Quantitative determination of the scattering and absorption coefficients from diffuse reflectance and transmittance measurements: application to pharmaceutical powders, Appl. Spectrosc. 51 (1997) 309–317, https://doi.org/10.1366/0003702971940404.

[65] D.J. Dahm, K.D. Dahm, Representative layer theory for diffuse reflectance, Appl. Spectrosc. 53 (1999) 647–654, https://doi.org/10.1366/0003702991947298.

[66] T. Burger, H.J. Ploss, J. Kuhn, S. Ebel, J. Fricke, Diffuse reflectance and transmittance spectroscopy for the quantitative determination of scattering and absorption coefficients in quantitative powder analysis, Appl. Spectrosc. 51 (1997) 1323–1329, https://doi.org/10.1366/0003702971941999.

[67] S. Landi, I.R. Segundo, E. Freitas, M. Vasilevskiy, J. Carneiro, C.J. Tavares, Use and misuse of the Kubelka-Munk function to obtain the band gap energy from diffuse reflectance measurements, Solid State Commun. 341 (2022) 1–7, https://doi.org/10.1016/j.ssc.2021.114573.

[68] G. Férey, Hybrid porous solids: past, present, future, Chem. Soc. Rev. 37 (2008) 191–214, https://doi.org/10.1039/b618320b.

[69] M.A. Nasalevich, C.H. Hendon, J.G. Santaclara, K. Svane, B. Van Der Linden, S. L. Veber, M.V. Fedin, A.J. Houtepen, M.A. Van Der Veen, F. Kapteijn, A. Walsh, J. Gascon, Electronic origins of photocatalytic activity in d0 metal organic frameworks, Sci. Rep. 6 (2016) 1–9, https://doi.org/10.1038/srep23676.

[70] P.H.M. Andrade, N. Henry, C. Volkringer, T. Loiseau, H. Vezin, M. Hureau, A. Moissette, Iodine uptake by Zr-/Hf-Based UiO-66 materials: the influence of

metal substitution on iodine evolution, ACS Appl. Mater. Interfaces (2022), https://doi.org/10.1021/acsami.2c07288.
[71] J. Heine, K. Müller-Buschbaum, Engineering metal-based luminescence in coordination polymers and metal-organic frameworks, Chem. Soc. Rev. 42 (2013) 9232–9242, https://doi.org/10.1039/c3cs60232j.
[72] P. Huo, T. Chen, J. Le Hou, L. Yu, Q.Y. Zhu, J. Dai, Ligand-to-ligand charge transfer within metal-organic frameworks based on manganese coordination polymers with tetrathiafulvalene-bicarboxylate and bipyridine ligands, Inorg. Chem. 55 (2016) 6496–6503, https://doi.org/10.1021/acs.inorgchem.6b00571.
[73] C. Xu, Y. Pan, G. Wan, H. Liu, L. Wang, H. Zhou, S.H. Yu, H.L. Jiang, Turning on visible-light photocatalytic C-H oxidation over metal-organic frameworks by introducing metal-to-cluster charge transfer, J. Am. Chem. Soc. 141 (2019) 19110–19117, https://doi.org/10.1021/jacs.9b09954.
[74] C.A. Kent, D. Liu, L. Ma, J.M. Papanikolas, T.J. Meyer, W. Lin, Light harvesting in microscale metal-organic frameworks by energy migration and interfacial electron transfer quenching, J. Am. Chem. Soc. 133 (2011) 12940–12943, https://doi.org/10.1021/ja204214t.
[75] M.A. Nasalevich, M.G. Goesten, T.J. Savenije, F. Kapteijn, J. Gascon, Enhancing optical absorption of metal-organic frameworks for improved visible light photocatalysis, Chem. Commun. 49 (2013) 10575–10577, https://doi.org/10.1039/c3cc46398b.
[76] P.H.M. Andrade, M. Moreau, N. Henry, M.T. Bakouche, S. Duval, C. Volkringer, T. Loiseau, M. Hureau, A. Moissette, Raman mapping as a tool for evaluating I2 and I3- diffusion over single-crystal UiO-67_NH2(M) (M = Zr, Zr/Hf, or Hf), J. Phys. Chem. C 2 (2022), https://doi.org/10.1021/acs.jpcc.2c08723.
[77] P.H.M. Andrade, H. Ahouari, C. Volkringer, T. Loiseau, H. Vezin, M. Hureau, A. Moissette, Electron-donor functional groups, band gap tailoring, and efficient charge separation: three keys to improve the gaseous iodine uptake in MOF materials, ACS Appl. Mater. Interfaces 15 (2023) 31032–31048, https://doi.org/10.1021/acsami.3c04955.
[78] T. Ahnfeldt, N. Guillou, D. Gunzelmann, I. Margiolaki, T. Loiseau, G. Férey, J. Senker, N. Stock, [Al4(OH)2(OCH3)4(H2N-Bdc)3]·xH2O: a 12-connected porous metal-organic framework with an unprecedented aluminum-containing brick, Angew. Chem. Int. Ed. 48 (2009) 5163–5166, https://doi.org/10.1002/anie.200901409.
[79] J.H. Cavka, S. Jakobsen, U. Olsbye, N. Guillou, C. Lamberti, S. Bordiga, K. P. Lillerud, A new zirconium inorganic building brick forming metal organic frameworks with exceptional stability, J. Am. Chem. Soc. 130 (2008) 13850–13851, https://doi.org/10.1021/ja8057953.
[80] M. Dan-Hardi, C. Serre, T. Frot, L. Rozes, G. Maurin, C. Sanchez, G. Férey, A new photoactive crystalline highly porous titanium(IV) dicarboxylate, J. Am. Chem. Soc. 131 (2009) 10857–10859, https://doi.org/10.1021/ja903726m.
[81] S. Jakobsen, D. Gianolio, D.S. Wragg, M.H. Nilsen, H. Emerich, S. Bordiga, C. Lamberti, U. Olsbye, M. Tilset, K.P. Lillerud, Structural determination of a highly stable metal-organic framework with possible application to interim radioactive waste scavenging: Hf-UiO-66, Phys. Rev. B Condens. Matter Mater. Phys. 86 (2012) 1–11, https://doi.org/10.1103/PhysRevB.86.125429.
[82] M.J. Katz, Z.J. Brown, Y.J. Colón, P.W. Siu, K.A. Scheidt, R.Q. Snurr, J.T. Hupp, O.K. Farha, A facile synthesis of UiO-66, UiO-67 and their derivatives, Chem. Commun. 49 (2013) 9449–9451, https://doi.org/10.1039/C3CC46105J.
[83] M. Leloire, C. Walshe, P. Devaux, R. Giovine, S. Duval, T. Bousquet, S. Chibani, J. Paul, A. Moissette, H. Vezin, P. Nerisson, L. Cantrel, C. Volkringer, T. Loiseau, Capture of gaseous iodine in isoreticular zirconium-based UiO-n metal-organic frameworks: influence of amino functionalization, DFT calculations, Raman and EPR spectroscopic investigation, Chem. Eur. J 28 (2022), https://doi.org/10.1002/chem.202104437 e202104437.
[84] S. Hu, M. Liu, K. Li, Y. Zuo, A. Zhang, C. Song, G. Zhang, X. Guo, Solvothermal synthesis of NH2-MIL-125(Ti) from circular plate to octahedron, CrystEngComm 16 (2014) 9645–9650, https://doi.org/10.1039/c4ce01545b.
[85] A.Y. Galashev, A.S. Vorob'ev, Physical properties of silicene electrodes for Li-, Na-, Mg-, and K-ion batteries, J. Solid State Electrochem. 22 (2018) 3383–3391, https://doi.org/10.1007/s10008-018-4050-8.
[86] K. Hendrickx, D.E.P. Vanpoucke, K. Leus, K. Lejaeghere, A. Van Yperen-De Deyne, V. Van Speybroeck, P. Van Der Voort, K. Hemelsoet, Understanding intrinsic light absorption properties of UiO-66 frameworks: a combined theoretical and experimental study, Inorg. Chem. 54 (2015) 10701–10710, https://doi.org/10.1021/acs.inorgchem.5b01593.
[87] L.M. Yang, E. Ganz, S. Svelle, M. Tilset, Computational exploration of newly synthesized zirconium metal-organic frameworks UiO-66, -67, -68 and analogues, J. Mater. Chem. C 2 (2014) 7111–7125, https://doi.org/10.1039/c4tc00902a.
[88] A.S. Yasin, J. Li, N. Wu, T. Musho, Study of the inorganic substitution in a functionalized UiO-66 metal-organic framework, Phys. Chem. Chem. Phys. 18 (2016) 12748–12754, https://doi.org/10.1039/c5cp08070c.
[89] A. Wang, Y. Zhou, Z. Wang, M. Chen, L. Sun, X. Liu, Titanium incorporated with UiO-66(Zr)-type metal-organic framework (MOF) for photocatalytic application, RSC Adv. 6 (2016) 3671–3679, https://doi.org/10.1039/c5ra24135a.
[90] J. Tu, X. Zeng, F. Xu, X. Wu, Y. Tian, X. Hou, Z. Long, Microwave-induced fast incorporation of titanium into UiO-66 metal-organic frameworks for enhanced photocatalytic properties, Chem. Commun. 53 (2017) 3361–3364, https://doi.org/10.1039/c7cc00076f.
[91] S. Liu, Z. Ren, H. Xu, Y. Xing, X. Jin, G. Ni, Z. Wang, Visible-light-responsive NaBiO3/UiO-67 heterojunction with enhanced photocatalytic performance, Mater. Sci. Semicond. Process. 147 (2022) 106708, https://doi.org/10.1016/j.mssp.2022.106708.
[92] X. Zhao, M. Xu, X. Song, X. Liu, W. Zhou, H. Wang, P. Huo, Tailored linker defects in UiO-67 with high ligand-to-metal charge transfer toward efficient photoreduction of CO2, Inorg. Chem. 61 (2022) 1765–1777, https://doi.org/10.1021/acs.inorgchem.1c03690.
[93] E. Flage-Larsen, A. Røyset, J.H. Cavka, K. Thorshaug, Band gap modulations in UiO metal-organic frameworks, J. Phys. Chem. C 117 (2013) 20610–20616, https://doi.org/10.1021/jp405335q.
[94] S. Chavan, J.G. Vitillo, D. Gianolio, O. Zavorotynska, B. Civalleri, S. Jakobsen, M. H. Nilsen, L. Valenzano, C. Lamberti, K.P. Lillerud, S. Bordiga, H2 storage in isostructural UiO-67 and UiO-66 MOFs, Phys. Chem. Chem. Phys. 14 (2012) 1614–1626, https://doi.org/10.1039/c1cp23434j.
[95] S.Q. Wang, X. Wang, X.Y. Zhang, X.M. Cheng, J. Ma, W.Y. Sun, Effect of the defect modulator and ligand length of metal-organic frameworks on carbon dioxide photoreduction, ACS Appl. Mater. Interfaces 13 (2021) 61578–61586, https://doi.org/10.1021/acsami.1c21663.
[96] R. Raciti, R. Bahariqushchi, C. Summonte, A. Aydinli, A. Terrasi, S. Mirabella, Optical bandgap of semiconductor nanostructures: methods for experimental data analysis, J. Appl. Phys. 121 (2017) 234304, https://doi.org/10.1063/1.4986436.
[97] C. Rotaru, S. Nastase, N. Tomozeiu, Amorphous phase influence on the optical bandgap of polysilicon, Phys. Status Solidi 171 (1999) 365–370, https://doi.org/10.1002/(SICI)1521-396X(199901)171. :1<365::AID-PSSA365>3.0.CO;2-M.
[98] B. Gu, N.H. Kwong, R. Binder, Relation between the interband dipole and momentum matrix elements in semiconductors, Phys. Rev. B 87 (2013) 125301, https://doi.org/10.1103/PhysRevB.87.125301.
[99] B. Jensen, Quantum theory of the complex dielectric constant of free carriers in polar semiconductors, IEEE J. Quantum Electron. 18 (1982) 1361–1370, https://doi.org/10.1109/JQE.1982.1071713.
[100] P. Hervé, L.K.J. Vandamme, General relation between refractive index and energy gap in semiconductors, Infrared Phys. Technol. 35 (1994) 609–615, https://doi.org/10.1016/1350-4495(94)90026-4.
[101] H. Finkenrath, The Moss rule and the influence of doping on the optical dielectric constant of semiconductors–I, Infrared Phys. 28 (1988) 327–332, https://doi.org/10.1016/0020-0891(88)90054-1.
[102] T.S. Moss, Relations between the refractive index and energy gap of semiconductors, Phys. Status Solidi 131 (1985) 415–427, https://doi.org/10.1002/pssb.2221310202.
[103] N.M. Ravindra, P. Ganapathy, J. Choi, Energy gap-refractive index relations in semiconductors–an overview, Infrared Phys. Technol. 50 (2007) 21–29, https://doi.org/10.1016/j.infrared.2006.04.001.
[104] D.R. Penn, Wave-number-dependent dielectric function of semiconductors, Phys. Rev. 128 (1962) 2093–2097, https://doi.org/10.1103/PhysRev.128.2093.
[105] S.H. Wemple, Optical oscillator strengths and excitation energies in solids, liquids, and molecules, J. Chem. Phys. 67 (1977) 2151–2168, https://doi.org/10.1063/1.435102.
[106] P. George, P. Chowdhury, Complex dielectric transformation of UV-vis diffuse reflectance spectra for estimating optical band-gap energies and materials classification, Analyst 144 (2019) 3005–3012, https://doi.org/10.1039/c8an02257g.
[107] H.A. Kramers, The quantum theory of dispersion, Nature 114 (1924) 310–311, https://doi.org/10.1038/114310b0.
[108] R. de L. Kronig, On the theory of dispersion of X-rays, J. Opt. Soc. Am. 12 (1926) 547–557, https://doi.org/10.1364/JOSA.12.000547.
[109] A.B. Kuzmenko, Kramers–Kronig constrained variational analysis of optical spectra, Rev. Sci. Instrum. 76 (2005) 83108, https://doi.org/10.1063/1.1979470.
[110] E. Yablonovitch, Photonic band-gap structures, J. Opt. Soc. Am. B 10 (1993) 283–295, https://doi.org/10.1364/JOSAB.10.000283.